Remote Sensing of Environment 338 (2026) 115372

Contents lists available at ScienceDirect

Remote Sensing of Environment

journal homepage: www.elsevier.com/locate/rse

A low-cost passive corner reflector design for SAR and InSAR applications

S. Azadnejad [a,*], A. Trafford [a,b], F. O'Loughlin [a,b], E.P. Holohan [b,c], B. Dashwood [d], A. White [d], J. Chambers [d], S. Donohue [a,b]

[a] UCD School of Civil Engineering, University College Dublin, Dublin, Ireland
[b] SFI Research Centre in Applied Geosciences (iCRAG), University College Dublin, Dublin, Ireland
[c] UCD School of Earth Sciences, University College Dublin, Dublin, Ireland
[d] British Geological Survey, Keyworth, United Kingdom

ARTICLE INFO

Edited by Jing M. Chen

Keywords:
SAR
InSAR
Landslide
Corner reflectors
Low-cost materials

ABSTRACT

Passive corner reflectors, made typically of metal plates, are widely used as point targets in synthetic aperture radar (SAR) and SAR interferometry (InSAR) applications. Drawbacks of such corner reflectors include: (i) high cost, especially when many reflectors are required for monitoring purposes; (ii) creation of localised ground motion in soft or unstable soils; and (iii) attractiveness for thieves. We tested several lower-cost and lighter weight materials for making corner reflectors. A cubic trihedral corner reflector, made of 2 mm thick aluminium plates, served as a standard. It was compared to corner reflectors built from 10 mm thick multiwall polycarbonate sheets covered with: (a) nothing; (b) c. 0.1 mm thick aluminium tape; or (c) aluminium-bearing metallic paint. In Sentinel-1 SAR backscatter imagery, the corner reflectors made of aluminium and polycarbonate sheets covered with aluminium tape (PC-AT) were equally visible. In contrast, the plain polycarbonate sheet and the polycarbonate sheet with aluminium paint were invisible. Scanning electron microscope (SEM) analysis of tape microstructure showed a well-distributed and dense layer of aluminium particles, which provides good dielectric response and high visibility in SAR imagery. Furthermore, a PC-AT corner reflector installed on an active landslide site yielded not only highly coherent pixels, but also displacement time series that were closely correlated with temporal variations of in-situ ground properties, such as soil moisture and matric suction. In terms of material cost and weight, the PC-AT corner reflector is approximately 94% cheaper and 71% lighter than the aluminium corner reflector, based on current market prices in Ireland. These low-cost, light-weight PC-AT corner reflectors are thus suitable for operational use in SAR- and InSAR-based monitoring.

1. Introduction

Corner reflectors are artificial installations at specific locations that reflect radar or other electromagnetic waves towards their emission source (Xia et al., 2022; Sarabandi and Chiu, 1996; Van Zyl and Jakob., 1990). There are two types of corner reflector: passive Corner reflectors, which lack electronics, and active Corner reflectors, so-called electronic CR (ECR) or compact transponders (CAT), which have electronic parts to amplify the incoming signals before being transmitted (Volakis and Volakis, 2007).

The use of corner reflectors was first aimed at the calibration of synthetic aperture radar (SAR) systems (Sarabandi and Chiu, 1996; Spencer, 1944; Van Zyl and Jakob., 1990). Corner reflectors have a high and stable radar cross section (RCS) and a well-defined scattering centre. Consequently, they are easily detectable in the image, which makes them suitable for SAR radiometric (Huang et al., 2022; Mishra et al., 2014; Schwerdt et al., 2017), geometric (Esposito et al., 2019; Gisinger et al., 2020; Jiao et al., 2023; Yang et al., 2020), and polarimetric calibration (Kumar et al., 2022; Tan and Hong, 2016; S. Wang et al., 2020).

Corner reflectors and transponders are also used for SAR interferometry (InSAR) datum connection and geodetic integration (Collilieux et al., 2022; Czikhardt et al., 2021; Gruber et al., 2022; Kalia et al., 2017; P. Mahapatra et al., 2018; Papco et al., 2024). InSAR datum connection is a process to transform spatially-relative InSAR displacement estimates (local datum) to a standard terrestrial reference frame (global datum) (P. Mahapatra et al., 2018). Corner reflectors or transponders have been integrated with Global Navigation Satellite System (GNSS) antennas to provide precise, absolute positioning in the global reference frame (P. Mahapatra et al., 2018). Corner reflectors are commonly used as point

* Corresponding author.
E-mail address: saeedazadnejad@gmail.com (S. Azadnejad).

https://doi.org/10.1016/j.rse.2026.115372
Received 14 August 2025; Received in revised form 21 February 2026; Accepted 13 March 2026
Available online 21 March 2026

targets in the monitoring of ground motion by Time-series InSAR (TS-InSAR) techniques (Ferretti et al., 2007; Qin et al., 2013; Talib et al., 2022). Such techniques provide a time-series of ground motion at mm-scale precision from a set of SAR images, and are widely used in various environmental monitoring applications (Saeed Azadnejad et al., 2024; Fu et al., 2025; Hrysiewicz et al., 2024; S. Zhao et al., 2024; C. Zhou et al., 2025). However, their use is challenging in areas of low interferometric coherence, which may be characterised by dense vegetation, snow, or glaciers (S Azadnejad et al., 2020; Michele Crosetto et al., 2016). One response to this challenge is to use computational approaches to increase the density of coherent points in InSAR analysis (S Azadnejad et al., 2023; S Azadnejad et al., 2025; Navneet et al., 2017; Y. Zhang et al., 2022). Another response is to deploy corner reflectors as artificial coherent scatters to obtain more localised but potentially more reliable measurement points (Darvishi et al., 2018; Friedt, 2024).

Corner reflectors have been already installed and tested places for different InSAR applications such as monitoring slope stability and landslide motion (Bovenga et al., 2017; M Crosetto et al., 2013; Guido Luzi et al., 2022; Schlögel et al., 2017; Shi et al., 2015; Singleton et al., 2014; Xia et al., 2022), tracking glacier flow and stability of snow covered sites (Friedt, 2024; Jauvin et al., 2019; Kaushik et al., 2022; G Luzi et al., 2020; Qiao et al., 2024), subsidence of mining areas (Gama et al., 2017; Pawłuszek-Filipiak et al., 2023; X.-m. Xing et al., 2013), highways and railways (Kelevitz et al., 2022a; X. Xing et al., 2018; X.M. Xing et al., 2016; Zhu, 2011) and other processes causing ground motion (Boukhemacha et al., 2021; Dheenathayalan et al., 2017; Rohmer et al., 2015; Talib et al., 2022; Xu Wang et al., 2024).

Passive corner reflectors are usually made of aluminium plates, with a large size with respect to radar wavelength (Doerry and Brock, 2009; Guido Luzi et al., 2022). For example, a triangular trihedral corner reflector should typically have an inner leg length of at least 1.5 m in order to be visible across the SAR frequency spectrum (X-, C-, and L-band) (Garthwaite, 2017). One significant drawback of using metal corner reflectors for InSAR applications is their high cost, especially when a large number of reflectors are required for monitoring purposes (Guido Luzi et al., 2022; Guido Luzi et al., 2021). In addition, heavy and bulky corner reflectors can cause localised ground motion, particularly in soft or unstable soils (Garthwaite, 2017; Jauvin et al., 2019). Moreover, metal corner reflectors are attractive targets for metal thieves, as they are often deployed in remote places and are difficult to secure.

Active transponders and electronic corner reflectors, with their compact and lightweight design, provide an effective solution to the size and weight challenges of passive metal corner reflectors (P.S. Mahapatra et al., 2013). However, due to the need for electronics, amplification, and power supply, they are generally more costly than passive corner reflectors (Garthwaite, 2017; Guido Luzi et al., 2021; P.S. Mahapatra et al., 2013). Despite some efforts to develop low-cost active corner reflectors, their price is still too high compared to passive corner reflectors (Guido Luzi et al., 2022; Guido Luzi et al., 2021; Guido Luzi et al., 2025).

In recent years, there have also been attempts to propose solutions to address the limitation of heavy and bulky passive metal corner reflectors. For instance,(Dheenathayalan et al., 2017) explored the use of small corner reflectors. They recommended the installation of a set of such CRs (c. 30 cm) in a pattern (like an arrow, for example) over an area of several 100 m^2 to enable their identification in the images. Signal processing techniques were also applied to improve the signal quality. However, the use of small corner reflectors presents several challenges: (i) their low signal-to-clutter ratio (SCR) would limit their applicability for medium-resolution SAR images from missions like Sentinel-1, (ii) the requirement to install multiple corner reflectors in a structured arrangement increases costs and labour for fabrication and deployment, and (iii) their deployment in specific patterns to enhance visibility may not always be practical in real-world applications.

To reduce material usage, researchers have proposed simplified aluminium corner reflector designs, such as triangular trihedral, trimmed square and rectangular and small semi-circular dihedral corner reflectors (Li et al., 2012; Guido Luzi et al., 2022; Qi et al., 2025; Xia et al., 2022). While these designs partially address the drawbacks of heavy and bulky corner reflectors, but their reduced size limits effectiveness for medium-resolution imaging. In addition, the high cost of aluminium still remains a barrier for large-scale deployment.

Therefore, a compromise solution needs to be taken for operational monitoring. The main objective of this paper is to investigate the use of alternative materials – multiwall polycarbonate sheets with various coatings - for making large, lightweight and cost-effective passive corner reflectors. In this regard, the visibility and backscattering properties of such materials when constructed into a corner reflector are assessed by using Sentinel-1C-band SAR images. To investigate its role on radar reflectivity, the microstructure of these materials was analysed using a scanning electron microscope (SEM). Field assessment of corner reflector performance was carried out at initially at a stable ground control site and subsequently at a site with known ground movement issues. Ultimately, we show that corner reflectors made of multiwall polycarbonate sheets with aluminium tape perform as well as corner reflectors made of aluminium metal plates, and so represent a viable low-cost, low weight design for operational InSAR-based ground motion monitoring.

2. Materials and methods

2.1. Design and development of corner reflectors

A cubic trihedral corner reflector was designed and assembled to carry out our analysis and investigations (Fig. 1a). The overall structure of this corner reflector is inspired by (Czikhardt et al., 2021). The design of our corner reflector consists of three plates set orthogonal to each other; two lower plates measure 1500 × 750 mm and a third plate sitting half-way along these plates and at right angles to them measures 750 mm × 750 mm. Once orientated correctly in the field, this corner reflector design works for both ascending (east-north-east looking) and descending (west-southwest looking) satellite orbits.

Corner reflectors are typically mounted on concrete pillars that are anchored into the ground (Czikhardt et al., 2021; Friedt, 2024; Yu et al., 2013). However, high levels of labour and cost are needed for such installation approaches. In this study, a simple method for deploying corner reflectors is proposed, where our corner reflector is attached to a four-legged supporting frame (Fig. 1b) that is driven into the ground.

2.2. Corner reflectors materials

A corner reflector made of 2-mm-thick aluminium plates serves as a baseline for our analysis (Fig. 2a). It is compared to corner reflectors built from (a) 10 mm thick multiwall polycarbonate sheets (Fig. 2b), (b) multiwall polycarbonate sheets covered by c. 0.1 mm thick aluminium tape (Fig. 2c), and (c) multiwall polycarbonate sheets coated with metallic paint layer approximately 1 mm thick (Fig. 2d). For simplicity, the corner reflectors are referred to in terms of their materials as Aluminium (AL), PolyCarbonate (PC), PolyCarbonate sheets covered with Aluminium Tape (PC-AT), and PolyCarbonate sheets coated with Aluminium Paint (PC-AP) throughout the remainder of the paper.

When comparing materials based on cost per square metre, it was found that polycarbonate was roughly 94% cheaper than aluminium in terms of material cost per square metre. In addition, polycarbonate is significantly lighter, weighing about 1.5 kg/m^2 compared to aluminium's 5.4 kg/m^2—making it approximately 71% lighter. It is important to note that the relative price of aluminium and polycarbonate may vary by location and over time, and the comparison presented here corresponds to market rates in Ireland at the time of submission.

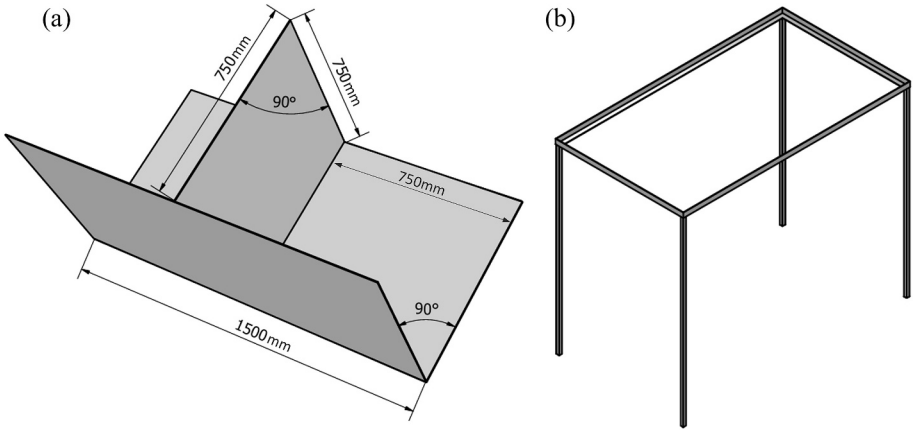

Fig. 1. 3D schematic of the corner reflector design. The design comprises: (a) the orthogonal plates, (b) the four-legged supporting frame.

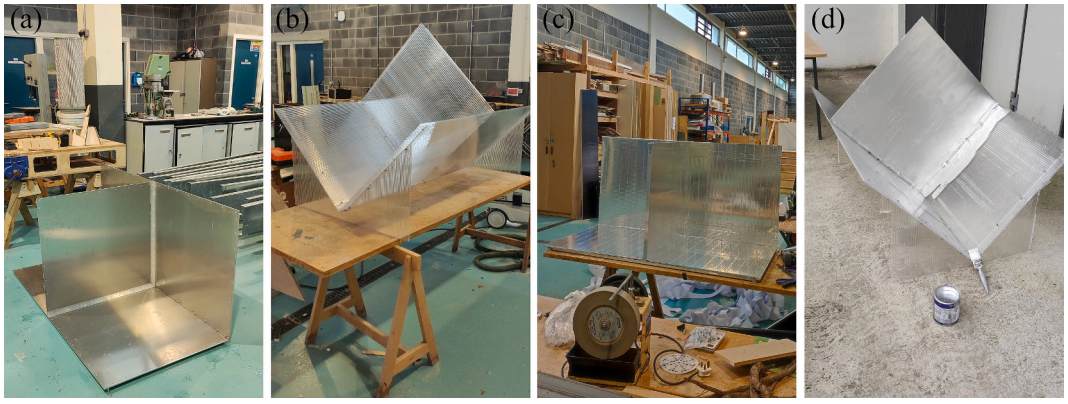

Fig. 2. Images of corner reflectors of various materials as tested in this study. The prototype corner reflectors were made of (a) aluminium plates, (b) multiwall polycarbonate sheets, (c) multiwall polycarbonate sheets covered by aluminium tape, or (d) multiwall polycarbonate sheets coated with aluminium paint.

2.3. On-site installation of corner reflectors

2.3.1. Stable site – UCD rosemount

To assess their SAR response, corner reflectors made of different materials were set up at a low SAR reflectivity site - the Rosemount Environmental Research Station at University College Dublin (Fig. 3b). The corner reflector was fixed to the four-legged support frame using screws. Each leg of the frame was driven 30 cm into the ground by hammering, and the frame was levelled after installation. The frame was set at 1 m above ground level to minimise unwanted ground reflections (Fig. 3c). The corner reflector and frame were orientated east-west, such that the middle upright plate was aligned north-south (Fig. 3d). The same frame was used for all corner reflectors (Fig. 3d-g).

2.3.2. Unstable site – Hollin Hill

After testing the visibility and response of the corner reflectors in Sentinel-1 images of a stable area, one AL corner reflector and one PC-AT corner reflector (i.e. one of each) were installed at the Hollin Hill Landslide Observatory (Fig. 4). This landslide site is located between longitudes 0.962° - 0.958°W and latitudes 54.1100° - 54.115°N, about 2 km southeast of the village of Terrington in North Yorkshire in the UK (Fig. 4b). The Hollin Hill site has been used as a landslide research site for testing a range of geophysical characterisation and monitoring methods for more than twenty years (Chambers et al., 2011; Uhlemann et al., 2017; Wacquier et al., 2021). The hillside has a slope angle of c.12°, with landslides extending for many hundreds of metres along the valley; the distance between the top of the slope and the valley floor is approximately 200 m (see Fig. 4c, d). The style of movement transitions from rotational sliding, which forms a set of arcuate headwall scarps at the upper end, through to translational sliding in the mid-section and finally to a set of four slump-like lobes at its toe. Failure occurs within a 20–30 m thick, formation of fissile mudstone and siltstone (the Whitby Mudstone Formation of Jurassic age), which gently dips to the North, and outcrops through the centre of the landslide area (Chambers et al., 2008; Jenkins et al., 2006).

The study area has pockets of dense vegetation within fenced enclosures, which presents a challenge for InSAR analysis due to the lack of natural coherent pixels. To overcome this, six square trihedral corner reflectors made of three orthogonal but trimmed aluminium plates, each with 0.7 m edge length and a thickness of 3 mm, were previously installed by the British Geological Survey (BGS) in July 2019 to monitor ground motions related to the landslide and to ground settlement (see Fig. 4b, e, f) (Kelevitz et al., 2022b). They were all orientated towards the ascending satellite viewing geometry.

To avoid interference between the previously-installed and newly-installed corner reflectors, our corner reflectors (the AL and PC-AT – installed 12-05-2024) were located several 10s of metres to the east of the pre-existing corner reflector array (see Fig. 4b, g, i). The same installation procedure as the UCD Rosemount site was followed. The legs of the frame housing the corner reflector were driven c. 300 mm into the ground. Drainage holes (5 mm diameter) were drilled into the bases of the corner reflectors to prevent the build-up of water during heavy rainfall.

At both corner reflector locations, soil moisture sensors and matric suction sensors (Fig. 4h) were installed at the same date (12-05-2024) in the shallow subsurface to support interpretation of the derived ground

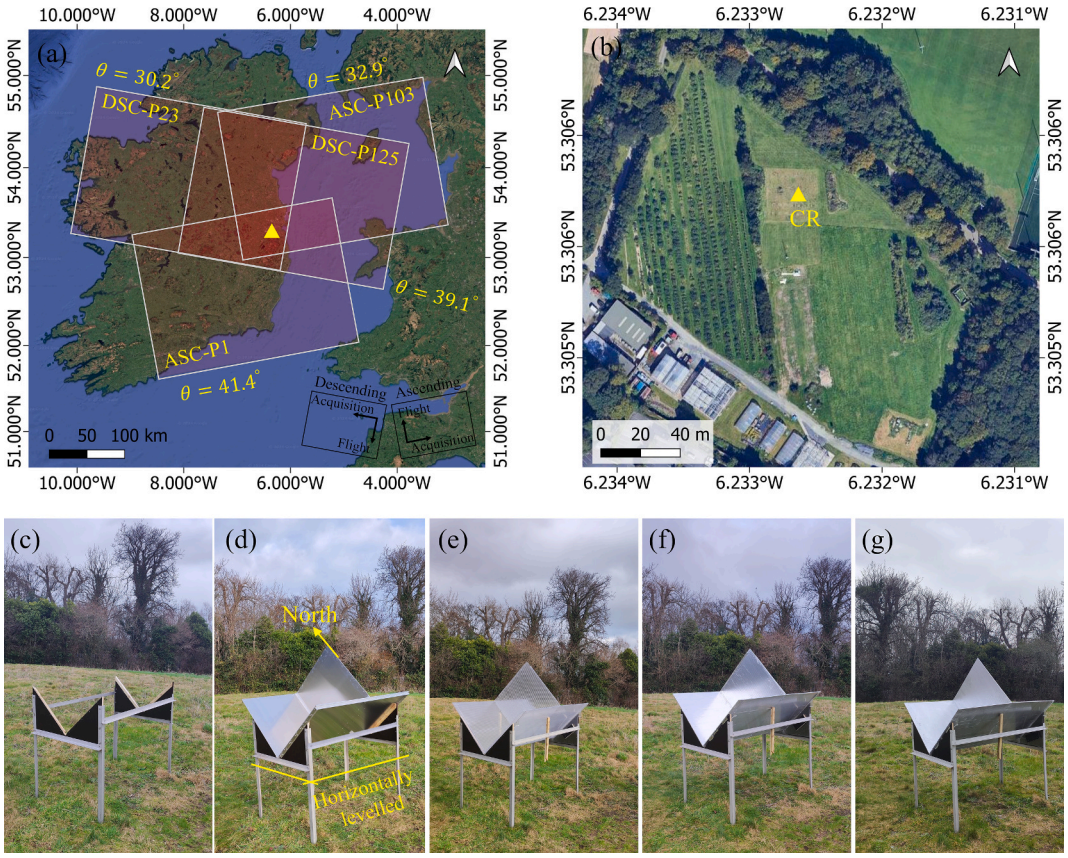

Fig. 3. Overview of SAR satellite imaging geometry and corner reflector installation at the stable UCD Rosemount test site. (a) Footprints of ascending (paths 1 and 103) and descending (paths 23 and 125) Sentinel-1 images that cover the location of CR (marked with a yellow triangle). θ is the local incidence angle. (b) Close-up view of the control site in Rosemount Environmental Research Station, University College Dublin, where the CRs were installed and tested. (c) A four-legged table was anchored into the ground and levelled horizontally at a height of 1 m above the ground. (d) The AL corner reflector was installed on 28-11-2023. (e) The PC corner reflector was installed on 02-02-2024. (f) The PC-AT corner reflector was installed on 13-02-2024. (g) The PC-AP corner reflector was installed on 08-03-2024. (For interpretation of the references to colour in this figure legend, the reader is referred to the web version of this article.)

motion time-series from InSAR analysis. A METER Group Terros 12 soil moisture sensor was paired with a METER Group Terros 21 soil water potential (matric suction) sensor, and both were installed at 0.5 m below ground level at each location. A second pair of soil moisture and matric suction sensors was installed at 1 m below ground level at each location. Both sensor types also record soil temperature at each of these depths. The sensor data were used to assess changes in soil properties at these depth levels that may affect the ground movement – e.g. due to shrinking and swelling of the clay soils.

2.4. Radar cross section of corner reflectors

The Radar Cross Section (RCS) is a measure of a target's ability to reflect radar signals towards a radar system (Graham and Harris, 2003). It is influenced by different factors such as the physical properties of the target (e.g., size, geometry, and material properties) and the radar system's characteristics (e.g., incidence angle, frequency, and polarization) (Ullah et al., 2024).

Corner reflectors should have dominant and insensitive RCS compared to the surrounding environment. The expected RCS value of corner reflectors of different shapes can be simulated analytically by using the formulas listed in Table 1, assuming they are made of metal (Qin et al., 2013).

For example, in our case, the expected RCS of a metal square trihedral, with an inner length of L = 0.75 m, in Sentinel-1 images with λ=0.056 m, is 3803.646 m^2, equivalent to 35.8 dBm^2 in logarithmic measure (i.e., $10log_{10}$).

2.5. SAR and InSAR processing

2.5.1. SAR intensity processing

Essential InSAR pre-processing steps, which include co-registration, merging, geocoding and cropping, are carried out using the InSAR Scientific Computing Environment (ISCE) software package on Sentinel-1 SLC data. The Sentinel-1 tracks covering the UCD Rosemount and Hollin Hill test sites are shown in Fig. 3 and Fig. 4, respectively.

The Sigma Nought ($\sigma_\circ$) and Beta Nought ($\beta_\circ$) backscattering coefficients are calculated from the pre-processed SLC images as follows (Miranda et al., 2015):

$$\sigma_\circ = \frac{|DN|^2}{A_\sigma{}^2} \tag{1}$$

$$\beta_\circ = \frac{|DN|^2}{A_\beta{}^2} \tag{2}$$

where DN is digital number or amplitude of the pixel. In the case of SLC data, amplitude of the pixel is defined as $DN = \sqrt{I^2 + Q^2}$, where I and Q are the real and imaginary parts of the backscattered complex signal respectively. A_β and A_β are calibration factors that are usually given in metadata of SAR imagery products in Single Look Complex (SLC) format.

The measured RCS coefficient is then estimated from the Beta Nought images using the 'Peak' estimation method as follows (Czikhardt et al., 2021; Gray et al., 2002; Ulander, 1991):

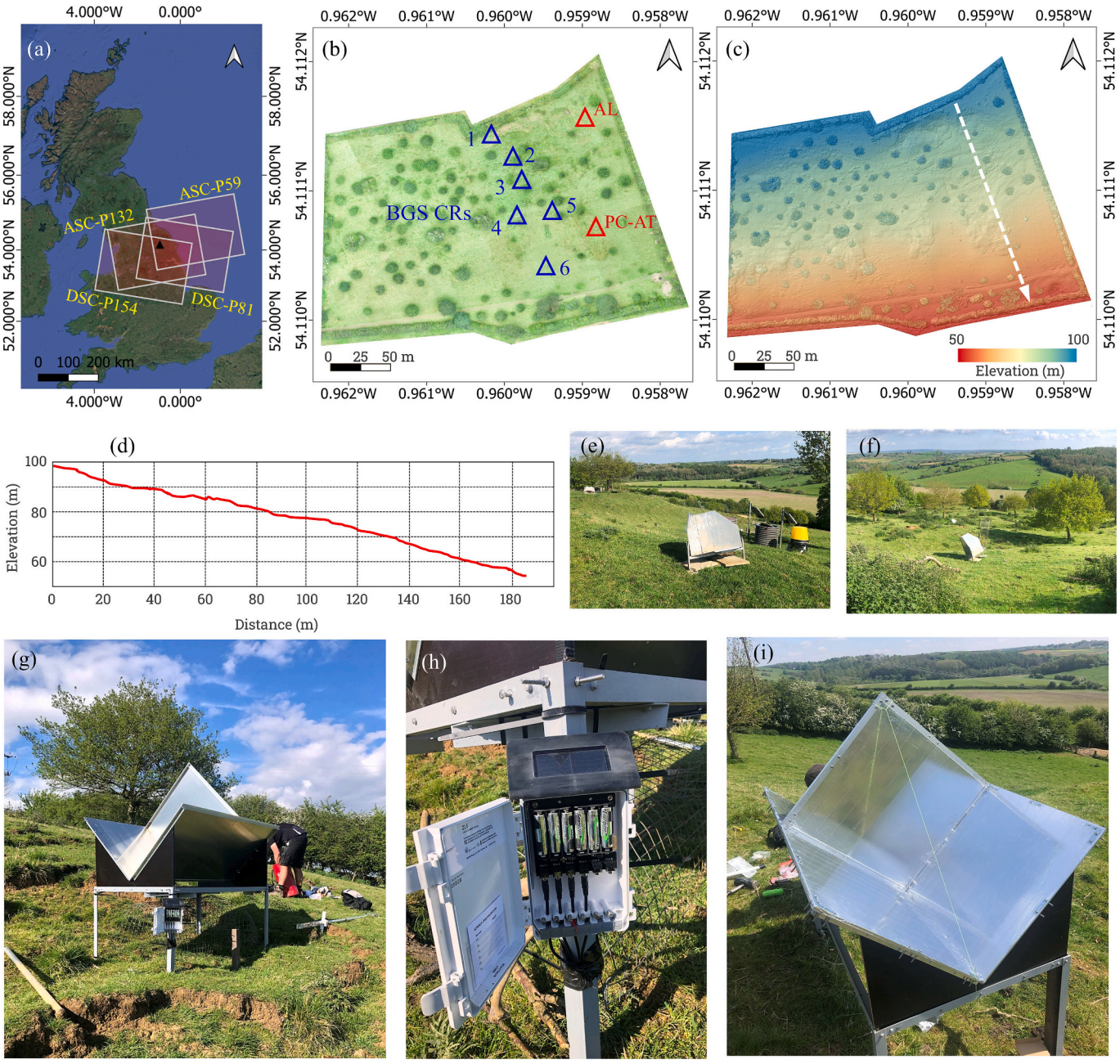

Fig. 4. Overview of SAR satellite imaging geometry and corner reflector installation at the unstable Hollin Hill test site. (a) Footprints of ascending (paths 59 and 132) and descending (paths 81 and 154) Sentinel-1 images over Hollin Hill landslide observatory (marked with a black triangle). (b) High resolution (10 cm) orthophoto (RGB) image of the Hollin Hill test site derived based on data acquired during the 06 July 2024 campaign. The blue triangles show the locations of six corner reflectors installed in July 2019 by British Geological Survey (BGS). The red triangles indicate the location of the AL and the PO-AT corner reflectors installed on 12-05-2024. (c) Digital Surface Model (DSM) of the Hollin Hill test site derived based on data acquired during the 06 July 2024 campaign. The DSM data was generated by BGS from drone-based LiDAR surveys using a DJI Zenmuse L1 sensor mounted on a DJI Matrice 300 RTK platform. (d) Profile of elevation along the specific section of the landslide, indicated by the white arrow in (c). (e) and (f) are example pictures of the BGS corner reflectors. (g) Indicates a photo of the AL corner reflector (h) Soil moisture and soil suction measurements are noted using ZL6 Data logger attached to each corner reflector. (i) Depicts a photo of the PO-AT corner reflector. (For interpretation of the references to colour in this figure legend, the reader is referred to the web version of this article.)

$$\mathrm{RCS} \approx \beta_{\circ} \times \Delta_{az}\Delta_{r} \tag{3}$$

where Δ_{az} and Δ_{r} are the azimuth and slant range pixel resolutions respectively.

The measured RCS of corner reflectors may vary from the ideal (theoretical) value due to unavoidable inherent fabrication errors. Comparing the observed RCS with the theoretical RCS is thus important for validating the performance of deployed corner reflectors under real-world conditions.

2.5.2. InSAR processing

The overall process workflow, including InSAR preprocessing and InSAR time series analysis, is shown in Fig. 5. All SLC images were coregistered and resampled to a common reference image using the ISCE. The coregistered SLCs are loaded into the Miami Phase Linking software in Python (MiaplPy (Mirzaee and Amelung, 2022)) package to generate the input format of SARvey software, an open-source InSAR package for local-scale ground motion detection (Piter et al., 2024). The SARvey is then applied to perform InSAR time series analysis.

Table 1
Theoretical RCS of the most common corner reflectors, where w and h are the width and length of the rectangle, λ is the wavelength of the transmitted radar signal, and L is the inner/side length of the corner reflector.

Type of corner reflectors	Maximum RCS (m^2)
Rectangular dihedral	$\frac{8\pi w^2 h^2}{\lambda^2}$
Triangular trihedral	$\frac{4\pi L^4}{3\lambda^2}$
Square trihedral	$\frac{12\pi L^4}{\lambda^2}$
Circular trihedral	$\frac{15.6\pi L^4}{\lambda^2}$

Interferograms are generated based on a small temporal baseline network. A set of first-order points were selected based on the temporal phase coherence approach (F. Zhao and Mallorqui, 2019), with a temporal coherence higher than 0.9. Potential outliers among the first-order points are identified and removed based on temporal unwrapping coherence within the spatial network (Piter et al., 2024). Phase unwrapping in time and space was carried out on the first-order points (Bioucas-Dias and Valadao, 2007; Boykov and Kolmogorov, 2004). The interferogram network is inverted to retrieve the displacement time series of the first-order points. The atmospheric phase screen (APS) is estimated from the displacement time series of the first-order points. A second-order points are also selected during this step based on a lower threshold (here defined as 0.8) on the temporal phase coherence computed for the selection of the first-order points. The estimated APS is interpolated to the location of the second-order points. The second-order points are added to the first-order points to densify the final set of points. The displacement time series are finally retrieved by unwrapping phases of the final set of points (Piter et al., 2024).

Independent displacement time series of the ascending and descending datasets are combined to derive vertical (up–down) and horizontal (east–west) components of ground motion. InSAR phase observations represent the projection of the 3-D displacement vector onto the radar line-of-sight (LoS) direction (Hanssen, 2001). This projection, d_{LoS}, in a Cartesian east, north, up coordinate system is defined as (Hanssen, 2001):

$$d_{\mathrm{LoS}} = [\sin\theta\sin\alpha \;\; \sin\theta\cos\alpha \;\; \cos\theta\,]\, d_{\mathrm{ENU}} \tag{4}$$

where $d_{\mathrm{ENU}} = [d_e d_n d_u]^T$ is the 3D displacement vector in east, north, and up direction, respectively. θ and α are the local incidence angle and local azimuth angle.

A decomposition of the LoS displacement vector into three orthogonal directions would require at least three independent LoS observations from significantly different viewing geometries (Brouwer and Hanssen, 2023; Qi et al., 2025). When only two LoS observation sets (i.e., ascending and descending) are available, this problem is typically handled under the assumption of negligible north-south motions (Fuhrmann and Garthwaite, 2019; Hanssen, 2001; Pepe et al., 2016). Therefore, this problem can be simplified as follows (Czikhardt et al., 2021; Ketelaar, 2009):

$$\begin{bmatrix} d_{\mathrm{asc}} \\ d_{\mathrm{dsc}} \end{bmatrix} = A.\begin{bmatrix} d_u \\ d_e \end{bmatrix}; A = \begin{bmatrix} \cos\theta_{asc} & \sin\theta_{asc}\sin\alpha_{asc} \\ \cos\theta_{dsc} & -\sin\theta_{dsc}\sin\alpha_{dsc} \end{bmatrix} \tag{5}$$

3. Results and discussion

3.1. Visibility and RCS of corner reflectors in Sentinel-1 backscatter intensity imagery

The first experiment was to visually check the Sentinel-1 SAR intensity images to see if the corner reflectors could be identified (Fig. 6 and Fig. 7). As shown in Fig. 3, the first (AL) and the last (PC-AP) corner reflector types were installed at the UCD control site on 28-11-2023 and 08-03-2024, respectively. Sentinel-1 images, in ascending (paths 1 and 103) and descending (paths 23 and 125) orbits, acquired from August 2023 to March 2024 were therefore assessed for this test phase. The SAR images before and after installation are analysed for each of the four orbits. Sigma Naught values at the corner reflector location are low in the pre-installation images (Fig. 6b and Fig. 7b) with average values, computed in a 3×3 pixel window, of -10.3 and -11.3 dB for ascending (path 103) and descending (path 125) orbits, respectively.

After the installation of the AL corner reflector, the SAR intensity values increase markedly to $+11.7$ and $+12.5$ dB for 103 and 125 orbits, respectively, at the corner reflection's location. (Fig. 6c and Fig. 7c). Note that 10–12 pixels in the SAR images are brightened by the presence of the aluminium corner reflector. These pixels represent a ground area of c. 500 m^2 – i.e. much greater than the <1 m^2 ground area occupied by the corner reflector. This phenomenon of 'bleeding' or 'spilling over' of the strongly reflected radar signal into the surrounding pixels is typical of an effective corner reflector (dominant radar scatterer).

The polycarbonate-only corner reflector type (PC) was not detected in Sentinel-1 images (Fig. 6d and Fig. 7d). Average Sigma Naught values of -10.8 dB and -13.8 dB, for orbits 103 and 125, respectively, were measured at the corner reflector location during this type's occupancy of the test site. These values are in line with background levels for the test site, which indicates that the polycarbonate sheets are transparent to Sentinel-1 radar signals.

In contrast, the corner reflector type made of polycarbonate plates covered with aluminium tape (PC-AT) was highly visible in the SAR images. The backscatter intensity values at the location of the corner reflector were significantly increased to $+10.2$ dB and $+10.5$ dB (Fig. 6e and Fig. 7e) while this corner reflector type was present there. This confirms that the transparency of the polycarbonate sheets to radar signals can be counteracted by adding a very thin conductive layer, such as aluminium tape.

Finally, the corner reflector type made of polycarbonate plates covered with aluminium paint (PC-AP) was not visible in Sentinel-1 images (Fig. 6f and Fig. 7f). Sigma Naught values of -11.9 dB and -12.6 dB for orbits 103 and 125, were measured at the location of the corner reflector while this type was present. This result shows that the radar signal passes through or reflects poorly off the aluminium paint, such that – at least as applied in this study – it's addition to the polycarbonate plates did not yield an effective corner reflector.

The time series of apparent RCS values at the corner reflector location for Sentinel-1 images shows a clear increase in RCS values after installation of the AL and PC-AT corner reflectors. The average RCS values of the AL and the PC-AT reflectors are 31.7 dBm^2 and 30.6 dBm^2,

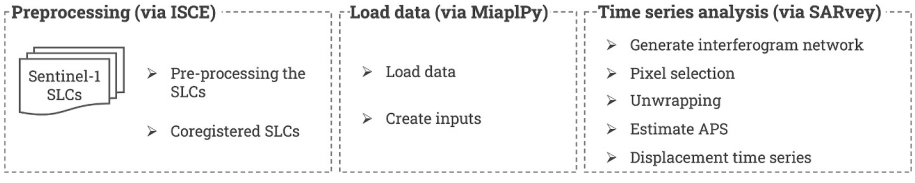

Fig. 5. Processing workflow for estimating InSAR displacement time series using ISCE, MiaplPy, and SARvey packages.

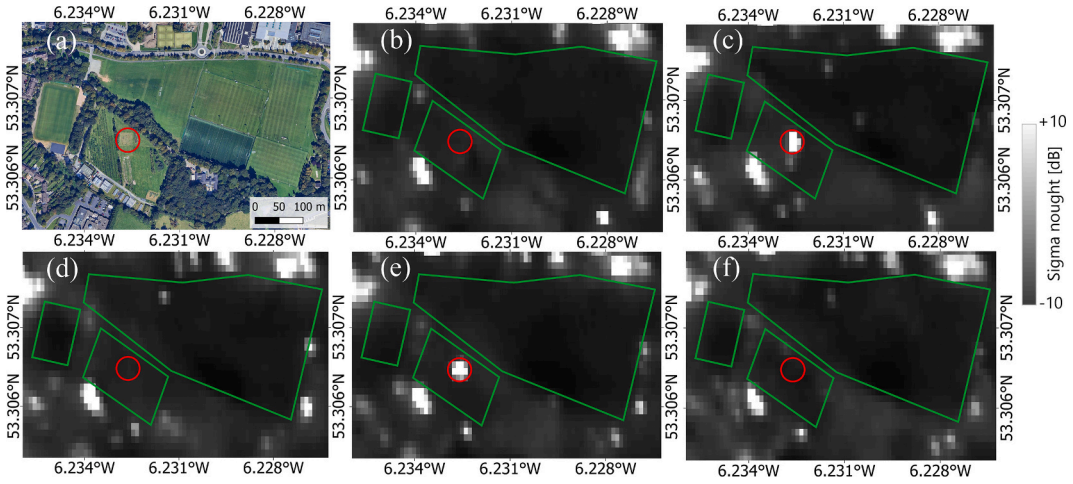

Fig. 6. Ascending-view visibility of tested corner reflectors in SAR backscatter intensity images. (a) Google map view of the area where the corner reflectors were installed (Google, Landsat / Copernicus / ©2024 TerraMetrics / ©2024 Airbus / ©2024 Maxar Technologies / IBCAO). The red circle shows the location of the installed corner reflector. Sigma Naught values expressed in dB on (b) 18-11-2023 before installation of the corner reflectors, (c) 30-11-2023 after installation of the AL corner reflector, (d) 10-02-2024 after installation of the PC corner reflector, (e) 22-02-2024 after installation of the PC-AT corner reflector, (f) 17-03-2024 PC-AP corner reflector. The Sigma Naught values were computed on Sentinel-1 images in ascending orbit (path 103). (For interpretation of the references to colour in this figure legend, the reader is referred to the web version of this article.)

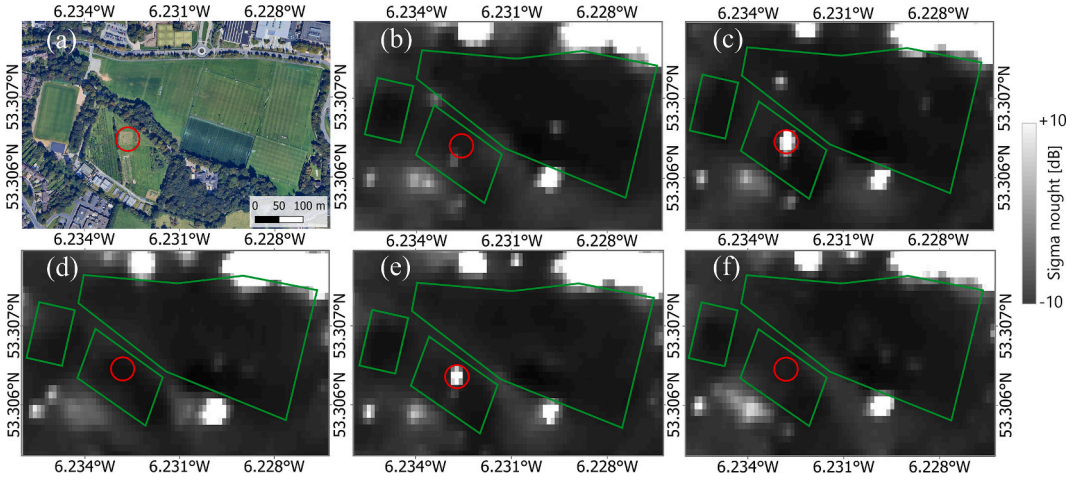

Fig. 7. Descending-view visibility of tested corner reflectors in SAR backscatter intensity images. (a) Google map view of the area where the CRs were installed (Google, Landsat / Copernicus / ©2024 TerraMetrics / ©2024 Airbus / ©2024 Maxar Technologies / IBCAO). The red circle shows the location of the installed CR. Sigma Naught values expressed in dB on (b) 20-11-2023 before installation of the corner reflectors, (c) 02-12-2023 after installation of the AL corner reflector, (d) 12-02-2024 after installation of the PC corner reflector, (e) 24-02-2024 after installation of the PC-AT corner reflector, (f) 19-03-2024 PC-AP corner reflector. The Sigma Naught values were computed on Sentinel-1 images in descending orbit (path 125). (For interpretation of the references to colour in this figure legend, the reader is referred to the web version of this article.)

respectively, which are 11–15% less than the theoretical value of 35.8 dBm^2. Since the design (roughness and shape), the installation process, and the installation location are the same, the difference in materials could be the main reason for the observed variation in the RCS values between the aluminium plate and aluminium tape.

Although the RCS values of the PC-AT corner reflector are slightly lower than the AL corner reflector, they seem to be more consistent over time (see Fig. 8). To investigate this, the correlation between the RCS values in ascending (paths 1 and 103) and descending (paths 23 and 125) orbits is plotted for the nearest dates (see Fig. 9). The correlation between the RCS values of the PC-AT corner reflector in ascending and descending orbits is higher than the AL corner reflector. As shown in Fig. 9, the PC-AT data (black and green markers) demonstrate a stronger and more consistent correlation of RCS values between ascending and descending orbits compared to the AL data (red and blue markers). This indicates that the PC-AT corner reflector is less affected by differences in acquisition geometry.

3.2. SEM analysis of corner reflectors materials

A microstructure analysis was carried out by using SEM on samples of the aluminium paint and the aluminium tape to see how the aluminium is organised in those materials at the micron scale. The aim of this test was to investigate why the aluminium paint, unlike the aluminium tape, fails to reflect radar signals back to the satellite. The results of the SEM analysis are provided in Fig. 10.

With the same level of magnification, SEM images reveal a relatively uniform particle size distribution for the aluminium tape. In addition, the tape contains considerably finer particles than the coarser particles observed in the paint.

Corner reflectors are usually made of high electrical conductive materials in order to provide strong backscattering in SAR images

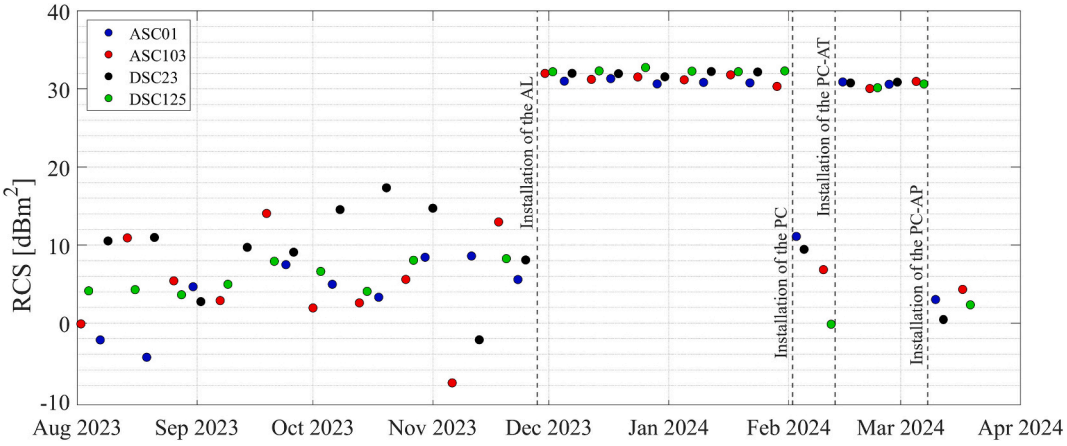

Fig. 8. Time series of measured Radar Cross Section (RCS) of the corner reflector location from Sentinel-1 images. Shown are data from in ascending (paths 1 and 103) and descending (paths 23 and 125) orbits. The black vertical dashed lines represent the date of installing the corner reflectors of various material types, including Aluminium (AL), PolyCarbonate (PC), PolyCarbonate sheets covered with Aluminium Tape (PC-AT), and PolyCarbonate sheets coated with Aluminium Paint (PC-AP).

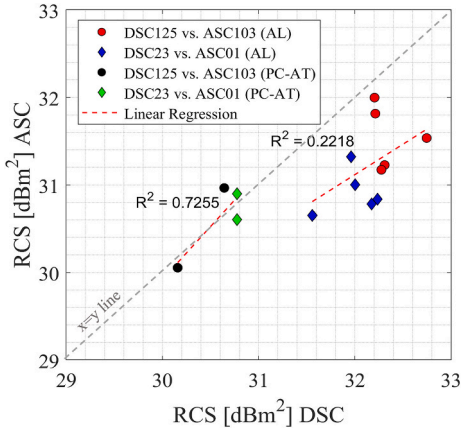

Fig. 9. Correlation between the RCS values in ascending (paths 1 and 103) and descending (paths 23 and 125) orbits for the nearest dates. The data points are colour-coded to distinguish comparisons: red and blue represent AL corner reflector, with red for RCS values in descending path 125 vs. its nearest date in ascending path 103 and blue for descending path 23 vs. its nearest date in ascending path 01. Black and green represent PC-AT corner reflector, with black for descending path 125 vs. its nearest date in ascending path 103 and green for descending path 23 vs. its nearest date in ascending path 01. (For interpretation of the references to colour in this figure legend, the reader is referred to the web version of this article.)

(Corona et al., 2000; Garthwaite, 2017; Mianroodi et al., 2016; Zheng et al., 2018). Aluminium foil/tape is a high electrical conductivity and low magnet permeability material (Ch and Shivamurthy, 2022; Luís et al., 2025; Silva et al., 2024; Y. Zhou et al., 2024). Therefore, the aluminium tape, with smooth and dense layer of aluminium particles, provide high electrical conductivity, resulting in a strong backscattering in SAR images. On the other hand, the aluminium paint with this large dispersion of aluminium particles within epoxy resin (visible as dark spaces between particles) may provide some degree of electrical conductivity, but it is insufficient to effectively reflect radar signals. This is because epoxy resin is non-conductive and significantly reduces electrical conductivity of aluminium paint (Krajewski et al., 2022; Lee and Kim, 2021; Xinyue Wang et al., 2023; W. Zhang et al., 2025).

3.3. Monitoring Hollin Hill landslide using corner reflectors

In the last experiment, the performance of the AL and PC-AT corner reflectors was assessed in an InSAR application to an area of unstable ground. Sentinel-1 images in ascending (path 132) and descending (paths 81) orbits, collected from May 2024 to Jan 2026, were used to analyse the backscattering and RSC of these corner reflectors. The AL and PC-AT corner reflectors were again both successfully detected in images acquired from the ascending and descending orbits (Fig. 11b and c). It was also observed that the BGS corner reflectors were only visible in the ascending pass as they were oriented towards the ascending geometry.

The two-year time series (Fig. 11d) reveals very high and relatively consistent backscatter amplitude, despite extreme weather events (e.g., minimum air temperature (mean, 30 min): −6 °C, wind speed (mean, 30 min): 17 m/s, maximum air temperature (mean, 30 min): 30 °C, daily rainfall 46 mm; historic climate data from the COSMOS weather station at the Hollin Hill landslide https://cosmos.ceh.ac.uk/). These results confirm the reliability of the reflector for long-term monitoring in challenging environmental conditions.

The backscatter amplitude values of the AL and PC-AT corner reflectors in the descending orbit are lower than those in the ascending orbit (Fig. 11d). Specifically, the average backscatter amplitude values for the AL and PC-AT corner reflectors in the ascending orbit are 60 dB and 61.27 dB, respectively. In the descending orbit, they are 57.23 dB and 56.99 dB, respectively. Since the Hollin Hill landslide is located on a south-facing slope (see Fig. 4c and d) the lower backscatter amplitude values in the descending orbit might be attributed to the orientation of the slope (Schaufler et al., 2018).

The backscatter amplitude values of the AL and PC-AT corner reflectors were compared with those of the BGS corner reflectors (Fig. 12). Since the BGS corner reflectors were orientated towards the ascending geometry (Kelevitz et al., 2022b), the comparison is conducted exclusively for the ascending (path 132) orbit. The mean backscatter amplitude values of our corner reflectors are higher than those of the BGS corner reflectors. The percentage difference between the mean backscatter amplitude value of our corner reflectors and lowest/highest mean backscatter amplitude values of the BGS corner reflectors is approximately 7% to 10%. The higher backscatter amplitude values of the AL and PC-AT corner reflectors are attributed to their larger size (0.75 m vs. 0.7 m) and differences in design, as the BGS corner reflectors were made using trimmed square plates.

Another difference observed was that our corner reflectors show smaller fluctuations, i.e., lower standard deviation values, compared to the BGS corner reflectors. This might be due to the different installation approaches used for our corner reflectors and the BGS corner reflectors. As shown in Fig. 4e and f, the BGS corner reflectors are just being placed

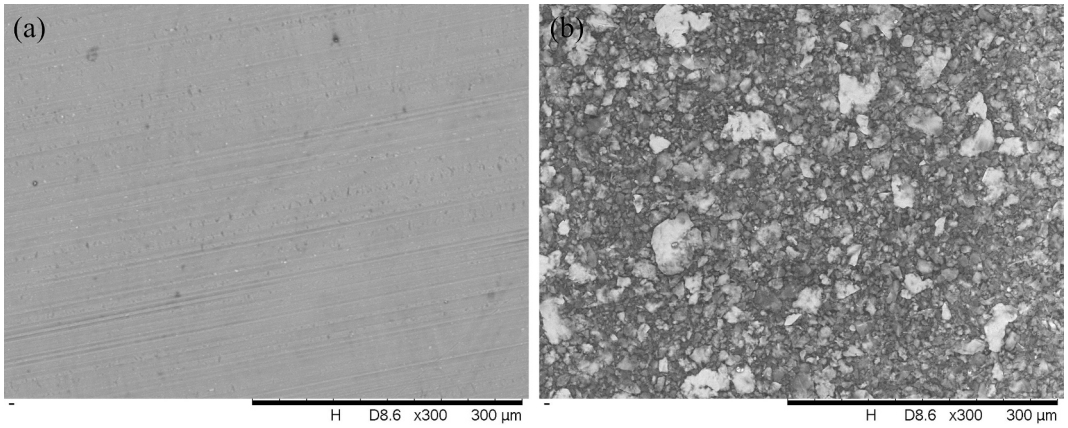

Fig. 10. SEM micrographs for (a) aluminium tape, and (b) aluminium paint.

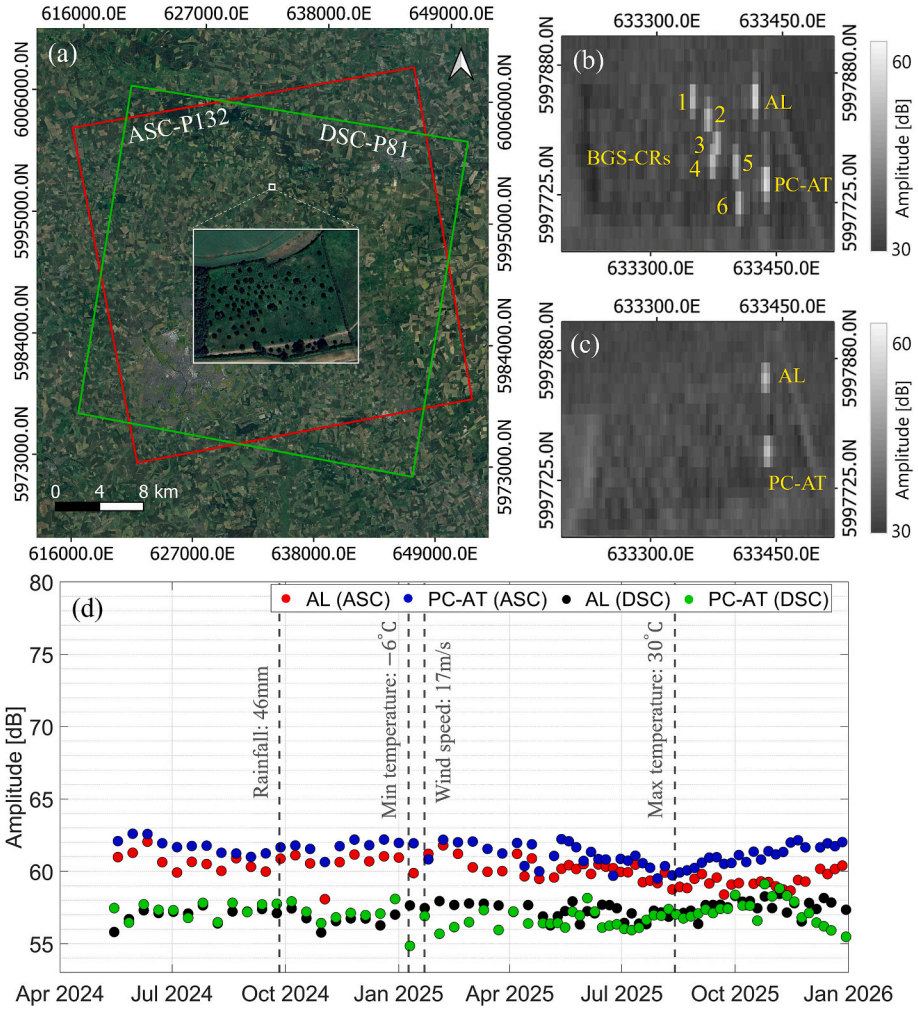

Fig. 11. Visibility of corner reflectors in SAR backscatter imagery of the unstable test site. (a) Area of interest in InSAR analysis for both descending (green rectangle) and ascending (red rectangle) orbits. Map of mean amplitude from SLC data in (b) ascending (path 132) and (c) descending (path 81) orbits over Hollin Hill landslide observatory. The BGS corner reflectors (1–6) are only seen in the ascending orbit as they were all oriented towards the ascending geometry. (d) Time series of backscatter amplitude of the AL corner reflector in ascending (red circles) and descending (black circles) and the PC-AT corner reflector in ascending (blue circles) and descending (green circles) orbits. (For interpretation of the references to colour in this figure legend, the reader is referred to the web version of this article.)

on the ground. In such situations, the undesired secondary reflections from the clutter can interfere with the corner reflector reflection. This indicates that proper installation is important to minimise external influences.

After assessing the backscattering of the AL and PC-AT corner reflectors, their performance in monitoring ground motion is assessed in relation to the Hollin Hill landslide. Line-of-sight (LOS) ground motion related to the landslide is measured for both ascending and descending

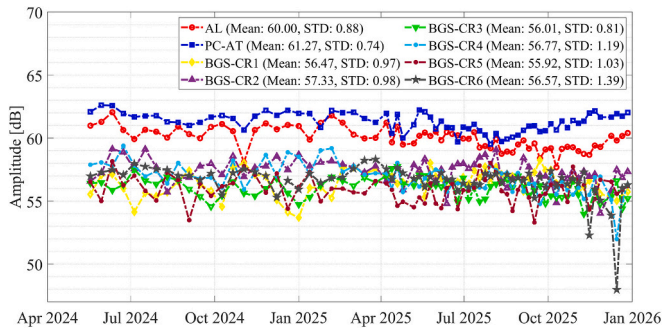

Fig. 12. Time series of backscatter amplitude of the corner reflectors. Mean and STD indicate the average and the standard deviation of the time series, respectively.

orbits based on interferograms with small temporal baselines (see Fig. 13).

Figure 14depicts the LOS displacement time-series of the AL and PC-AT corner reflectors for both ascending and descending orbits.

As illustrated in Fig. 14a and Fig. 14c, the general displacement trend of the AL corner reflector exhibits a similar pattern in both in ascending and descending orbits but with different amplitudes of change. Two drops can be seen in the time series during summer 2024 and summer 2025, reaching approximately −16 mm and − 40 mm in the ascending time series, compared to −10 mm and − 24 mm in the descending observations, respectively. Similarly, the PC-AT corner reflectors show similar temporal trends in both in ascending and descending orbits (Fig. 14b and Fig. 14d), but again with differing magnitudes. In the ascending, downward displacements of approximately −19 mm in summer 2024 and − 50 mm in summer 2025 are observed, whereas the corresponding values in the descending time series are limited to about −11 mm and − 19 mm, respectively.

The systematic differences between ascending and descending displacement magnitudes suggest that the observed ground motion is not purely vertical but includes a horizontal motion component. A comparison between the AL and PC-AT corner reflectors indicates that their displacement time series follow a similar trend up to summer 2025. After this period, however, an upward motion is observed in both ascending and descending displacement time series of the PC-AT reflector (Fig. 14b and Fig. 14d). This upward motion, however, is not observed for the AL reflector (Fig. 14a and Fig. 14c).

The LOS measurements derived from the ascending and descending orbits are then decomposed into vertical (up-down) and horizontal (east-west) components. Fig. 15a and Fig. 15b indicate the up-down and east-west displacements associated with the AL and PC-AT corner reflectors over time.

As illustrated, a sharp downward displacement is observed during summer 2025 in the up-down displacement time series of both corner reflectors. This drop corresponds to displacements of −40 mm and − 45 mm in the AL and PC-AT corner reflectors, respectively. During summer 2024, the up-down displacement time series of the corner reflectors show smaller magnitudes of −16 mm and − 18 mm. Horizontal eastward motions are also observed during summer 2024 and summer 2025 in the east-west displacement time series of both corner reflectors. In the AL corner reflector, the maximum eastward motion is 6 mm and 17 mm in summer 2024 and summer 2025, respectively. The corresponding values for the PC-AT corner reflector are 9 mm and 24 mm.

The vertical ground motion in both AL and PC-AT corner reflectors was then compared with the measurement obtain from the in-situ soil suction and soil moisture sensors (Fig. 16a-d).

As illustrated in Fig. 16a-d, noticeable changes in suction and water content were, recorded during the summer and autumn periods of both 2024 and 2025. Time series of precipitation and temperature data (Fig. 16e) confirm dry spells, characterised by minimal precipitation, in both summers. The summer/autumn of 2025 (June to October) was comparatively dry when compared to the equivalent period in 2024, resulting in substantially higher soil suction and lower water content at both shallow (0.5 m) and deep (1 m) sensors across the slope (Fig. 16a-d). As expected, the shallower suction sensors exhibited greater suction than those at depth.

The more variable response observed by the shallow suction and water content sensors in summer 2025, is likely associated with the location of these sensors on the slope. This section of the slope lies close to the backscarp and is therefore more susceptible to the development of tension cracks, particularly during dry periods. Such features can facilitate rapid infiltration following rainfall events, leading to a quicker reduction in suction and corresponding increase in water content at shallow depth compared with other parts of the slope.

The periods of higher suction (and lower water content), in both 2024 and 2025, correspond closely to a high magnitude of downward displacement recorded by InSAR. Maximum downward ground motion of −16 mm in summer 2024 and − 40 mm in summer 2025 are observed in the displacement time-series of the AL corner reflector. The corresponding values in the displacement time-series of the PC-AT corner reflector are −18 mm and − 45 mm. The more pronounced suction

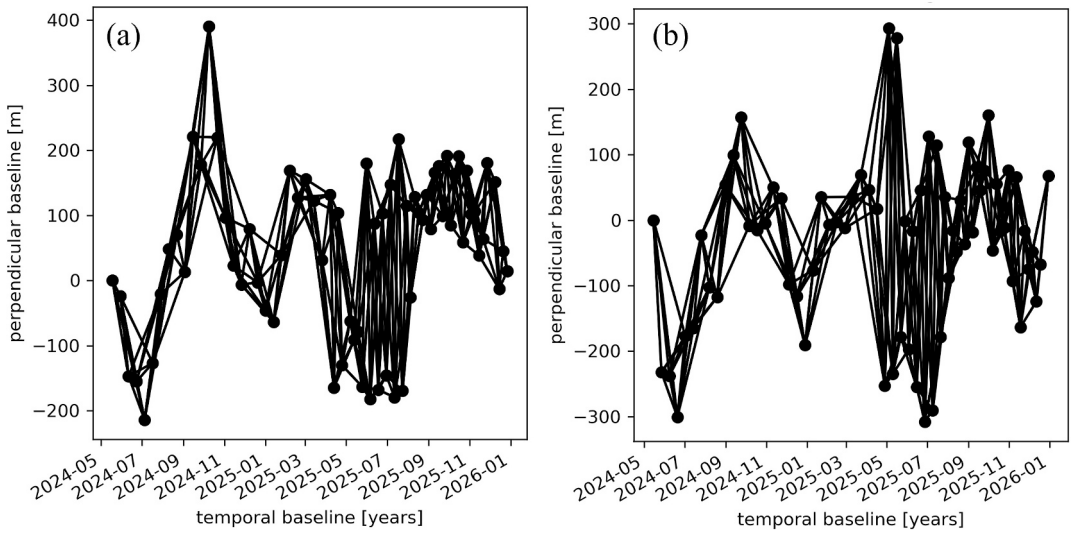

Fig. 13. Network of interferograms used for estimation of Hollin Hill ground motion in (a) ascending (path 132) and (b) descending (path 81) orbits.

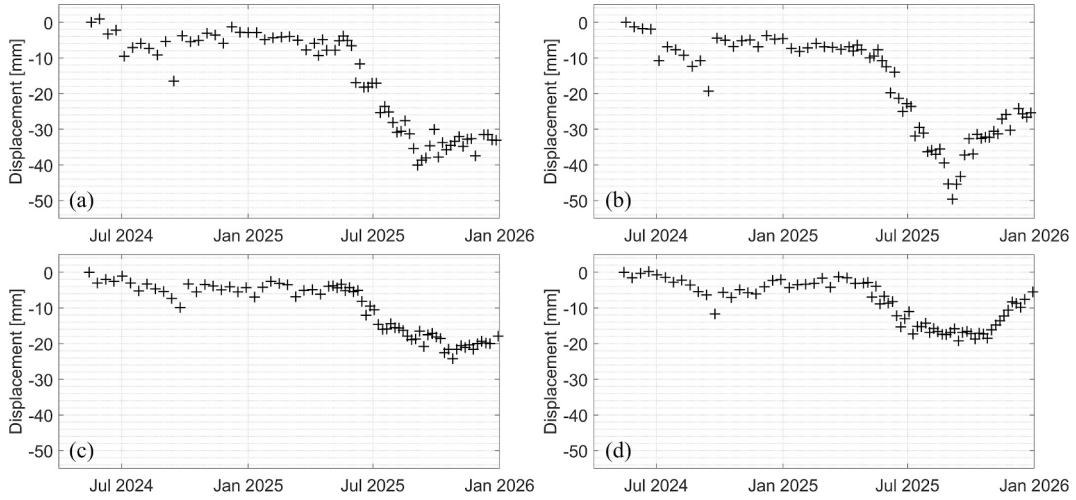

Fig. 14. The LOS displacements time-series of the pixel containing (a) the AL corner reflector in ascending (path 132), (b) the PC-AT corner reflector in ascending (path 132), (c) the AL corner reflector in descending (path 81), (d) the PC-AT corner reflector in descending (path 81), derived from Sentinel-1 images for the period of May 2024 to Jan 2026.

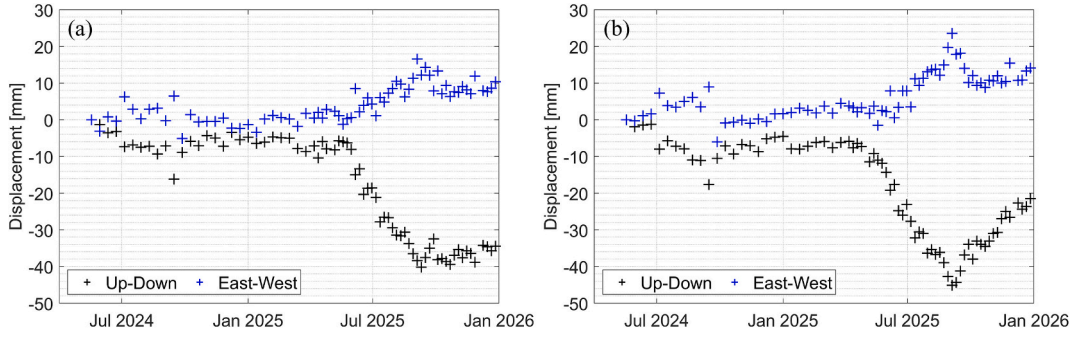

Fig. 15. Up-down and east-west displacements time series of the pixel containing (a) the AL corner reflector, and (b) the PC-AT corner reflector for the period of May 2024 to Jan 2026.

response at PC-AT is accompanied by a larger magnitude of downward displacement, indicating site-specific sensitivity to moisture loss.

A significant rainfall event on 26 September 2024 led to a swift recovery of suction and moisture levels to their pre-drying conditions. Similarly, a substantial rainfall event occurred on 20 September 2025, which also triggered a reduction in suction and partial recovery of soil moisture. The displacement time-series of the AL and PC-AT corner reflectors show consistent behaviour with these hydrological patterns. In summer 2024, a clear upward (recovery) displacement is observed following the late-September rainfall. In contrast, as of January 2026, the recovery in ground motion following the significant displacements observed in summer/autumn 2025 is incomplete, and this is particularly evident in the displacement record of the AL corner reflector, suggesting that permanent slope movement has occurred.

Overall, these results suggest that the observed vertical motion measured at the corner reflectors are predominantly associated with the shrinkage and swelling of the soil, caused by soil moisture variations during the dry and wet periods. The slope material, Whitby mudstone, is known to be susceptible to moisture-related volume change (Hobbs et al., 2012).

3.4. Error analysis of experimental data

An assessment of both random and systematic errors was conducted to evaluate the reliability of the corner reflector measurements. Random errors were quantified by analysing temporal fluctuations in the time series of RCS and backscatter intensity. As shown in Fig. 11d and Fig. 12, all reflectors exhibit some degree of variability; however, the magnitude of this variability differs between reflector types. The PC-AT corner reflector consistently exhibits lower temporal variability compared to the BGS corner reflectors. Specifically, the standard deviation of the RCS time series for the PC-AT reflector is approximately 9–47% lower than lowest/highest standard deviation of the BGS reflectors (Fig. 12). The aluminium reflector shows a similar level of stability to the PC-AT, indicating that the aluminium tape coating does not introduce additional noise relative to a solid aluminium surface.

Systematic differences in backscatter intensity were evaluated by comparing measurements from ascending and descending Sentinel-1 orbits. As can be seen in Fig. 11d, the backscatter intensity values of the PC-AT in the descending orbit are lower than those of the ascending orbit. To check if this difference represents a systematic bias, Sentinel-1 Ground Range Detected (GRD) data from all available ascending (paths 132 and 59) and descending (paths 81 and 154) orbits, covering the PC-AT corner reflector, were analysed using the Google Earth Engine platform (Gorelick et al., 2017). Fig. 17 depicts the time series of backscatter intensity for the PC-AT in the ascending (paths 132 and 59) and descending (paths 81 and 154) orbits.

The local incidence angle of the PC-AT in the available orbits, along with the statistical metrics of the time series shown in Fig. 17, are summarised in Table 2.

A difference of approximately 2.3–3.9 dB is observed between the mean intensity values of the ascending and descending orbits. The results indicate that this offset is primarily controlled by acquisition geometry rather than reflector performance. The statistics presented in

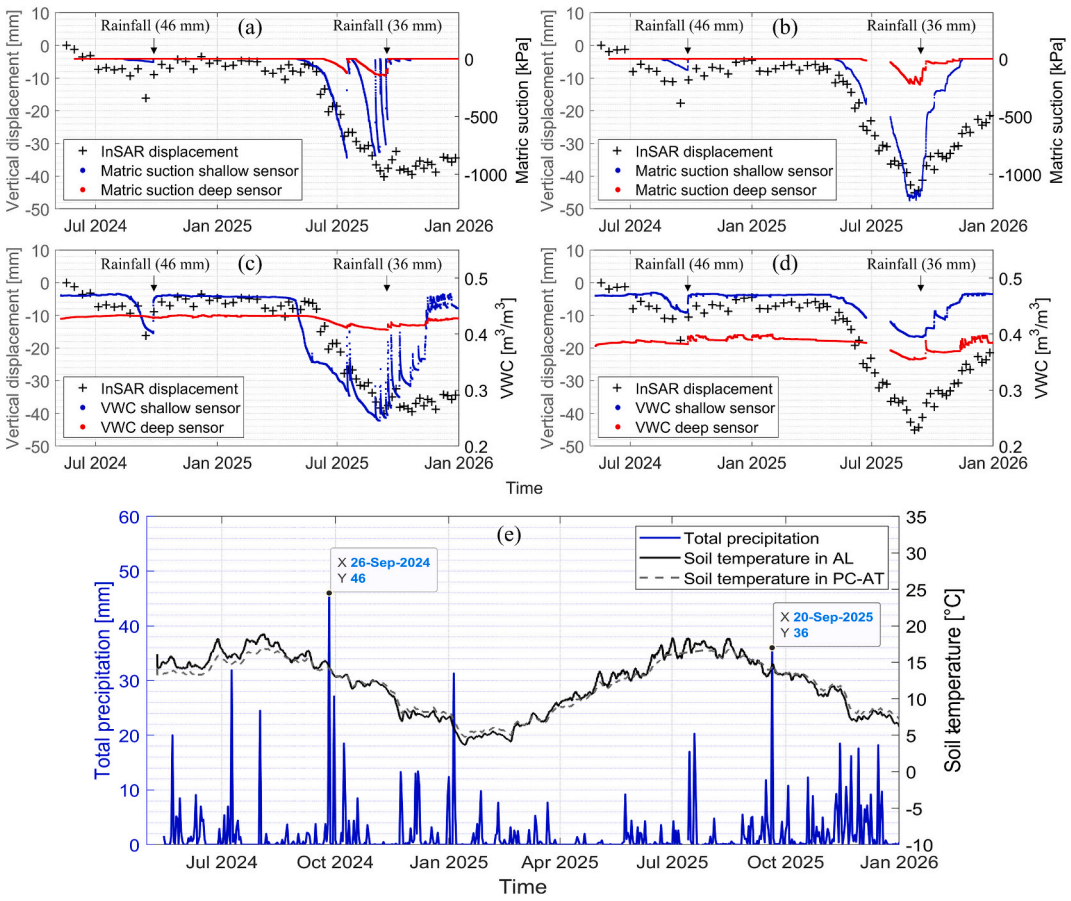

Fig. 16. Comparison of InSAR-derived up-down displacement time-series with soil suction and volumetric water content (VWC). InSAR-derived up-down displacement versus matric suction for (a) the AL corner reflector, and (b) the PC-AT corner reflector. InSAR-derived up-down displacement versus VWC for (c) the AL corner reflector, and (d) the PC-AT corner reflector. (e)Variation of precipitation and soil moisture temperature at the location of the AL and PC-AT corner reflectors. Precipitation data obtained from the COSMOS weather station at the Hollin Hill landslide.

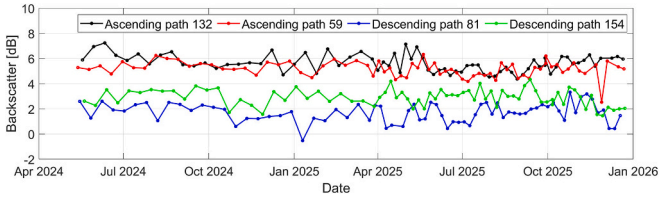

Fig. 17. Time series of backscatter intensity for the PC-AT corner reflector in ascending (paths 132 and 59) and descending (paths 81 and 154) orbits.

Table 2
Geometric characteristics of Sentinel-1 SAR acquisitions (e.g., local incidence angles) over the PC-AT corner reflector for ascending (paths 132 and 59) and descending (paths 81 and 154) orbits. Mean and standard deviation of backscatter intensity from May 2024 to December 2025 are also provided for each dataset.

Orbit (path)	Local incidence angle	Mean intensity	Std intensity
Ascending (132)	38.7°	5.64 dB	0.67
Ascending (59)	30.1°	5.17 dB	0.59
Descending (81)	43.2°	1.70 dB	0.75
Descending (154)	35.3°	2.90 dB	0.65

Table 2 further show that random variability in backscatter intensity (quantified by the standard deviation) is generally higher at steeper local incidence angles. Specifically, the highest standard deviations (0.75 dB) occur at the steepest angle (43.2°). This indicates that measurements taken at steeper viewing geometries (higher local incidence angles) are more sensitive to random noises.

3.5. Limitations of the research

This study serves as a proof-of-concept, with field testing limited to two sites: a stable, level-ground test site (UCD Rosemount) and an active landslide (Hollin Hill). However, the performance of the PC-AT reflector under other challenging monitoring scenarios remains to be evaluated. Conditions such as dense vegetation, snow cover, or extreme weather may affect both long-term durability and radar response.

The performance evaluation was conducted using C-band Sentinel-1 data. The effectiveness of the PC-AT design at other common SAR frequencies (e.g., X-band and L-band) remains untested. Since radar wavelength influences penetration depth, scattering mechanisms, and sensitivity to surface roughness, further investigations are required to substantiate the performance of the PC-AT corner reflector at different wavelengths.

The study focused on a cubic trihedral design with a fixed size (inner leg length of 0.75 m). Other reflector types, such as dihedral or triangular trihedral, were not tested. For instance, applying the PC-AT material to simplified designs (such as trimmed square and rectangular and small semi-circular dihedral corner reflectors) proposed in prior research (Li et al., 2012; Guido Luzi et al., 2022; Qi et al., 2025; Xia et al., 2022), could further optimise cost and deployment ease, particularly for dense networks or challenging terrains.

Overall, while the proposed low-cost PC-AT corner reflector design shows strong potential for operational InSAR monitoring, further long-

term, multi-site, and multi-frequency validation is recommended to fully characterise its robustness and limitations.

4. Summary and conclusions

In this study, polycarbonate plates coated with aluminium paint or tape were investigated as potential low-cost and lightweight materials for making cost-effective passive corner reflectors. This investigation included: (1) assessing their visibility and backscattering properties in Sentinel-1 SAR images; (2) analysing the microstructure of these materials; and (3) evaluating their performance in monitoring earth movements via InSAR at an active landslide site. The materials were incorporated into the same corner reflector design, consisting of three orthogonal plates: two lower plates measuring 1500 × 750 mm, and a third plate (750 × 750 mm) mounted perpendicularly across them. This geometry ensures functionality for both ascending and descending Sentinel-1 orbits. For ease of deployment, the corner reflectors were mounted on a four-legged table driven into the ground, offering a low-cost alternative to traditional concrete foundations.

The main findings of the study are as follows:

i. Polycarbonate plates coated with a thin but continuous metallic layer, such as aluminium tape, are highly reflective of C-band SAR signals and form suitable materials for the construction of passive corner reflectors. For the same corner reflector design, the performance of such plates in terms of SAR reflectivity is close to that solid aluminium plates.
ii. According to the SEM analysis, the density and uniformity of aluminium particles in the aluminium-bearing materials are identified as influential parameters in SAR reflectivity. The smooth and dense layer of aluminium particles in aluminium tape results in a strong backscattering in SAR images. A thin coat of aluminium paint, with large dispersion of aluminium particles within an epoxy resin, fails to reflect radar signals.
iii. The thickness of aluminium plates is not a significant factor in the SAR reflectivity of a corner reflector. Even a very thin but continuous aluminium layer, such as in aluminium tape, can produce backscattering comparable to that of thick aluminium plates. Increasing the plate thickness only adds to the cost and weight of the corner reflectors without greatly enhancing reflectivity.
iv. The PC-AT corner reflectors are also as effective as aluminium-only plates for InSAR-related applications. At the Hollin Hill landslide test site, a clear temporal correlation is observed between InSAR ground motion and soil suction and soil moisture over time for both corner reflector types. Meteorological and soil temperature data indicate that the InSAR-defined downward motion corresponded to the drying (shrinkage), while subsequent upward motion is associated with the wetting (swelling) of the soil.
v. The PC-AT corner reflectors are thus suitable as a lower-cost, lighter-weight alternative to solid aluminium corner reflectors for operational use in SAR- and InSAR-based monitoring.

CRediT authorship contribution statement

S. Azadnejad: Writing – original draft, Visualization, Validation, Software, Methodology, Investigation, Formal analysis, Data curation, Conceptualization. **A. Trafford:** Writing – review & editing, Methodology, Formal analysis. **F. O'Loughlin:** Writing – review & editing, Supervision. **E.P. Holohan:** Writing – review & editing, Supervision. **B. Dashwood:** Writing – review & editing, Resources, Data curation. **A. White:** Writing – review & editing, Resources, Data curation. **J. Chambers:** Writing – review & editing, Resources, Data curation. **S. Donohue:** Writing – review & editing, Supervision, Project administration, Investigation, Funding acquisition, Formal analysis.

Declaration of competing interest

The authors declare the following financial interests/personal relationships which may be considered as potential competing interests:

Saeed Azadnejad reports financial support was provided by Science Foundation Ireland. Saeed Azadnejad reports financial support was provided by Geological Survey of Ireland and the Environmental Protection Agency under the SFI Frontiers. Saeed Azadnejad reports a relationship with Science Foundation Ireland Public Fellowship Programme that includes: funding grants. If there are other authors, they declare that they have no known competing financial interests or personal relationships that could have appeared to influence the work reported in this paper.

Acknowledgements

The research described in this paper has been funded with the financial support of Research Ireland (formerly Science Foundation Ireland), Geological Survey Ireland and the Environmental Protection Agency under the SFI Frontiers for the Future Programme grant 19/FFP/6535. We would like to thank Matt Kirkham for collecting the drone data. B. Dashwood, A. White, and J. Chambers, publish with the permission of the Executive Director, British Geological Survey (UKRI-NERC).

Data availability

Data will be made available on request.

References

Azadnejad, S., Maghsoudi, Yasser, Perissin, Daniele, 2020. Evaluation of polarimetric capabilities of dual polarized Sentinel-1 and TerraSAR-X data to improve the PSInSAR algorithm using amplitude dispersion index optimization. Int. J. Appl. Earth Obs. Geoinf. 84, 101950.

Azadnejad, S., Esmaeili, M., Maghsoudi, Y., Donohue, S., Khoshlahjeh Azar, M., 2023. Extending polarimetric optimization of multi-temporal InSAR techniques on dual polarized Sentinel-1 data. Adv. Space Res. 72 (2), 349–360.

Azadnejad, Saeed, Hrysiewicz, Alexis, Trafford, Andrew, O'Loughlin, Fiachra, Holohan, E.P., Kelly, Fiona, Donohue, Shane, 2024. InSAR supported by geophysical and geotechnical information constrains two-dimensional motion of a railway embankment constructed on peat. Eng. Geol. 333, 107493.

Azadnejad, S., Kandiri, A., Hrysiewicz, A., O'Loughlin, F., Holohan, E.P., Dev, S., Donohue, S., 2025. Application of deep learning for coherent pixel selection in time series InSAR for urban area and transport infrastructure monitoring. Int. J. Appl. Earth Obs. Geoinf. 142, 104718.

Bioucas-Dias, Jos M., Valadao, Gonalo, 2007. Phase unwrapping via graph cuts. IEEE Trans. Image Process. 16 (3), 698–709.

Boukhemacha, Mohamed Amine, Teleaga, Delia, Serbulea, Manole-Stelian, Poncos, Valentin, Serpescu, Irina, Manoli, Daniel Marcel, Toma, Stefan-Adrian, Bica, Ioan, Haagmans, Roger, 2021. Combined in-situ and persistent Scatterers interferometry synthetic aperture radar (PSInSAR) monitoring of land surface deformation in urban environments-case study: tunnelling works in Bucharest (Romania). Int. J. Remote Sens. 42 (7), 2641–2662.

Bovenga, Fabio, Pasquariello, Guido, Pellicani, Roberta, Refice, Alberto, Spilotro, Giuseppe, 2017. Landslide monitoring for risk mitigation by using corner reflector and satellite SAR interferometry: the large landslide of Carlantino (Italy). Catena 151, 49–62.

Boykov, Yuri, Kolmogorov, Vladimir, 2004. An experimental comparison of min-cut/max-flow algorithms for energy minimization in vision. IEEE Trans. Pattern Anal. Mach. Intell. 26 (9), 1124–1137.

Brouwer, Wietske S., Hanssen, Ramon F., 2023. A treatise on InSAR geometry and 3-D displacement estimation. IEEE Trans. Geosci. Remote Sens. 61, 1–11.

Ch, R.B. Jagadeesh, Shivamurthy, B., Gowda, S.B. Bore, 2022. Flexible linear low-density polyethylene laminated aluminum and nickel foil composite tapes for electromagnetic interference shielding. Eng. Sci. 21 (5), 777.

Chambers, J.E., Weller, A.L., Gunn, D.A., Kuras, O., Wilkinson, P.B., Meldrum, P.I., Ogilvy, R.D., Jenkins, G.O., Gibson, A.D., Ford, S.J., 2008. Geophysical anatomy of the Hollin Hill Landslide, North Yorkshire, UK. In: Near Surface 2008-14th Eage European Meeting of Environmental and Engineering Geophysics.

Chambers, J.E., Wilkinson, P.B., Kuras, O., Ford, J.R., Gunn, D.A., Meldrum, P.I., Pennington, C.V.L., Weller, A.L., Hobbs, P.R.N., Ogilvy, R.D., 2011. Three-dimensional geophysical anatomy of an active landslide in Lias group mudrocks, Cleveland Basin, UK. Geomorphology 125 (4), 472–484.

Collilieux, Xavier, Courde, Clément, Fruneau, Bénédicte, Aimar, Mourad, Schmidt, Guillaume, Delprat, Isabelle, Defresne, Marie-Amélie, Pesce, Damien, Bergerault, Fabien, Wöppelmann, Guy, 2022. Validation of a corner reflector

installation at Côte D'azur multi-technique geodetic observatory. Adv. Space Res. 70 (2), 360–370.
Corona, P., D'agostino, Francesco, Riccio, Giovanni, Toso, G., 2000. Scattering from dihedral corner reflectors with sinusoidally deformed faces. Microw. Opt. Technol. Lett. 25 (4), 246–251.
Crosetto, M., Gili, J.A., Monserrat, O., Cuevas-González, M., Corominas, J., Serral, D., 2013. Interferometric SAR monitoring of the Vallcebre landslide (Spain) using corner reflectors. Nat. Hazards Earth Syst. Sci. 13 (4), 923–933.
Crosetto, Michele, Monserrat, Oriol, Cuevas-González, María, Devanthéry, Núria, Crippa, Bruno, 2016. Persistent scatterer interferometry: a review. ISPRS J. Photogramm. Remote Sens. 115, 78–89.
Czikhardt, Richard, Van Der Marel, Hans, Papco, Juraj, 2021. GECORIS: an open-source toolbox for analyzing time series of corner reflectors in InSAR geodesy. Remote Sens. 13 (5), 926.
Darvishi, Mehdi, Schlögel, Romy, Kofler, Christian, Cuozzo, Giovanni, Rutzinger, Martin, Zieher, Thomas, Toschi, Isabella, Remondino, Fabio, Mejia-Aguilar, Abraham, Thiebes, Benni, 2018. Sentinel-1 and ground-based sensors for continuous monitoring of the Corvara landslide (South Tyrol, Italy). Remote Sens. 10 (11), 1781.
Dheenathayalan, Prabu, Cuenca, Miguel Caro, Hoogeboom, Peter, Hanssen, Ramon F., 2017. Small reflectors for ground motion monitoring with InSAR. IEEE Trans. Geosci. Remote Sens. 55 (12), 6703–6712.
Doerry, Armin W., Brock, Billy C., 2009. Radar Cross Section of Triangular Trihedral Reflector with Extended Bottom Plate. Sandia Report, Sandia National Laboratory.
Esposito, C., Natale, A., Palmese, G., Berardino, P., Perna, S., 2019. Geometric distortions in FMCW SAR images due to inaccurate knowledge of electronic radar parameters: analysis and correction by means of corner reflectors. Remote Sens. Environ. 232, 111289.
Ferretti, Alessandro, Savio, Giuliano, Barzaghi, Riccardo, Borghi, Alessandra, Musazzi, Sergio, Novali, Fabrizio, Prati, Claudio, Rocca, Fabio, 2007. Submillimeter accuracy of InSAR time series: experimental validation. IEEE Trans. Geosci. Remote Sens. 45 (5), 1142–1153.
Friedt, Jean-Michel, 2024. Impact of a thin inhomogeneous snow layer on a microwave corner reflector RADAR cross section: consequences for spaceborne remote sensing. IEEE Trans. Geosci. Remote Sens. 62, 1–9.
Fu, Yuanzhao, Wang, Jili, Zhang, Yi, Yang, Honglei, Li, Lu, Ren, Zhengzhao, 2025. Spatiotemporal evolution characteristics of ground deformation in the Beijing plain from 1992 to 2023 derived from a novel multi-sensor InSAR fusion method. Remote Sens. Environ. 319, 114635.
Fuhrmann, Thomas, Garthwaite, Matthew C., 2019. Resolving three-dimensional surface motion with InSAR: constraints from multi-geometry data fusion. Remote Sens. 11 (3), 241.
Gama, Fábio F., Cantone, Alessio, Mura, José C., Pasquali, Paolo, Paradella, Waldir R., dos Santos, Athos R., Silva, Guilherme G., 2017. Monitoring subsidence of open pit iron mines at Carajás Province based on SBAS interferometric technique using TerraSAR-X data. Remote Sens. Appl.: Soc. Environ. 8, 199–211.
Garthwaite, Matthew C., 2017. On the design of radar corner reflectors for deformation monitoring in multi-frequency InSAR. Remote Sens. 9 (7), 648.
Gisinger, Christoph, Schubert, Adrian, Breit, Helko, Garthwaite, Matthew, Balss, Ulrich, Willberg, Martin, Small, David, Eineder, Michael, Miranda, Nuno, 2020. In-depth verification of Sentinel-1 and TerraSAR-X geolocation accuracy using the Australian corner reflector array. IEEE Trans. Geosci. Remote Sens. 59 (2), 1154–1181.
Gorelick, Noel, Hancher, Matt, Dixon, Mike, Ilyushchenko, Simon, Thau, David, Moore, Rebecca, 2017. Google earth engine: planetary-scale geospatial analysis for everyone. Remote Sens. Environ. 202, 18–27.
Graham, A.J., Harris, R., 2003. Extracting biophysical parameters from remotely sensed radar data: a review of the water cloud model. Prog. Phys. Geogr. 27 (2), 217–229.
Gray, A. Laurence, Vachon, Paris W., Livingstone, Charles E., Lukowski, Tom I., 2002. Synthetic aperture radar calibration using reference reflectors. IEEE Trans. Geosci. Remote Sens. 28 (3), 374–383.
Gruber, Thomas, Ågren, Jonas, Angermann, Detlef, Ellmann, Artu, Engfeldt, Andreas, Gisinger, Christoph, Jaworski, Leszek, Kur, Tomasz, Marila, Simo, Nastula, Jolanta, 2022. Geodetic SAR for height system unification and sea level research — results in the Baltic Sea test network. Remote Sens. 14 (14), 3250.
Hanssen, Ramon F., 2001. Radar Interferometry: Data Interpretation and Error Analysis, vol. 2. Springer Science & Business Media.
Hobbs, P.R.N., Entwisle, D.C., Northmore, K.J., Sumbler, M.G., Jones, L.D., Kemp, S., Self, S., Barron, M., Meakin, J.L., 2012. Engineering Geology of British Rocks and Soils: Lias Group.
Hrysiewicz, Alexis, Williamson, Jennifer, Evans, Chris D., Jonay Jovani-Sancho, A., Callaghan, Nathan, Lyons, Justin, White, Jake, Kowalska, Joanna, Menichino, Nina, Holohan, Eoghan P., 2024. Estimation and validation of InSAR-derived surface displacements at temperate raised peatlands. Remote Sens. Environ. 311, 114232.
Huang, Qiqi, Zhang, Fengli, Li, Lu, Liu, Xiaochen, Jiao, Yanan, Yuan, Xinzhe, Li, Huirong, 2022. Quick quality assessment and radiometric calibration of C-SAR/01 satellite using flexible automatic corner reflector. Remote Sens. 15 (1), 104.
Jauvin, Matthias, Yan, Yajing, Trouvé, Emmanuel, Fruneau, Bénédicte, Gay, Michel, Girard, Blaise, 2019. Integration of corner reflectors for the monitoring of mountain glacier areas with Sentinel-1 time series. Remote Sens. 11 (8), 988.
Jenkins, G.O., Jones, L.D., Gibson, A.D., 2006. Analysis of the Hollin Hill Landslide, Low Mowthorpe, North Yorkshire: Field Reconnaissance Survey and Proposed Survey Recommendations.
Jiao, Yanan, Zhang, Fengli, Liu, Xiaochen, Wang, Qi, Huang, Qiqi, Huang, Zhiwei, 2023. Preliminary evaluation of geometric positioning accuracy of C-SAR images based on automatic corner reflectors. Remote Sens. 15 (19), 4744.
Kalia, A.C., Frei, M., Lege, T., 2017. A Copernicus downstream-service for the nationwide monitoring of surface displacements in Germany. Remote Sens. Environ. 202, 234–249.
Kaushik, Suvrat, Leinss, Silvan, Ravanel, Ludovic, Trouve, Emmanuel, Yan, Yajing, Magnin, Florence, 2022. Monitoring hanging glacier dynamics from Sar images using corner reflectors and field measurements in the mont-blanc massif. ISPRS Ann. Photogram. Remote Sens. Spat. Inform. Sci. 3, 325–332.
Kelevitz, Krisztina, Novellino, Alessandro, Watlet, Arnaud, Boyd, James, Whiteley, James, Chambers, Jonathan, Jordan, Colm, Wright, Tim, Hooper, Andrew, Biggs, Juliet, 2022a. Ground and satellite-based methods of measuring deformation at a UK landslide observatory: comparison and integration. Remote Sens. 14 (12), 2836.
Kelevitz, Krisztina, Wright, Tim J., Hooper, Andrew J., Selvakumaran, Sivasakthy, 2022b. Novel corner-reflector array application in essential infrastructure monitoring. IEEE Trans. Geosci. Remote Sens. 60, 1–18.
Ketelaar, Virginia Bernardina Hendrika, 2009. Satellite Radar Interferometry: Subsidence Monitoring Techniques. Springer.
Krajewski, Dariusz, Oleksy, Mariusz, Oliwa, Rafał, Bulanda, Katarzyna, Czech, Kamil, Mazur, Damian, Masłowski, Grzegorz, 2022. Methods for enhancing the electrical properties of epoxy matrix composites. Energies 15 (13), 4562.
Kumar, Shashi, Babu, Arun, Agrawal, Shefali, Asopa, Udit, Shukla, Shashwat, Maiti, Abhisek, 2022. Polarimetric calibration of spaceborne and airborne multifrequency SAR data for scattering-based characterization of manmade and natural features. Adv. Space Res. 69 (4), 1684–1714.
Lee, Wondu, Kim, Jooheon, 2021. Highly thermal conductive and electrical insulating epoxy composites with a three-dimensional filler network by sintering silver nanowires on aluminum nitride surface. Polymers 13 (5), 694.
Li, Chengfan, Yin, Jingyuan, Zhao, Junjuan, Zhang, Guifang, Shan, Xinjian, 2012. The selection of artificial corner reflectors based on RCS analysis. Acta Geophys. 60 (1), 43–58.
Luís, Paulo, Martin-Fuentes, Silvia, Arnaiz, María, Ajuria, Jon, 2025. On the selection of the current collector for water processed activated carbon electrodes for their application in electrochemical capacitors. Batteries Supercaps 8 (2), e202400405.
Luzi, G., Fernandez, E., Mira Perez, F., Crosetto, M., 2020. A low cost active corner reflector to assist snow monitoring through sentinel/1 images. In: 2020 14th European Conference on Antennas and Propagation (EuCAP).
Luzi, Guido, Espín-López, Pedro F., Pérez, Fermín Mira, Monserrat, Oriol, Crosetto, Michele, 2021. A low-cost active reflector for interferometric monitoring based on sentinel-1 Sar images. Sensors 21 (6), 2008.
Luzi, Guido, Barra, Anna, Gao, Qi, Espín-López, Pedro F., Palamà, Riccardo, Monserrat, Oriol, Crosetto, Michele, Colell, Xavier, 2022. A low-cost active reflector and a passive corner reflector network for assisting landslide monitoring using multi-temporal InSAR. Remote Sens. Lett. 13 (11), 1080–1089.
Luzi, Guido, Gao, Qi, Espín-López, Pedro Fide, 2025. Experimental study of the stability of a low-cost C-Band active reflector using sentinel-1 imagery. IEEE Access. 13, 55202–55210.
Mahapatra, Pooja S., Samiei-Esfahany, Sami, van der Marel, Hans, Hanssen, Ramon F., 2013. On the use of transponders as coherent radar targets for SAR interferometry. IEEE Trans. Geosci. Remote Sens. 52 (3), 1869–1878.
Mahapatra, Pooja, van der Marel, Hans, van Leijen, Freek, Samiei-Esfahany, Sami, Klees, Roland, Hanssen, Ramon, 2018. InSAR datum connection using GNSS-augmented radar transponders. J. Geod. 92, 21–32.
Mianroodi, Yazdani, Reza, Hamid Heidar, Armaki, Hosein Mohseni, 2016. Expandable shipboard decoy including adequate RCS by using trihedral corner reflectors. IET Sci. Meas. Technol. 10 (5), 485–491.
Miranda, Nuno, Meadows, P.J., Type, D., Note, T., 2015. Radiometric calibration of S-1 level-1 products generated by the S-1 IPF. Viewed at https://sentinel. esa. int/documents/247904/685163/S1-Radiometric-Calibration-V1. 0. pdf.
Mirzaee, Sara, Amelung, Falk, Fattahi, Heresh, 2022. Non-linear phase linking using joined distributed and persistent scatterers. Comput. Geosci. 171, 105291.
Mishra, Mayank D., Patel, Parul, Srivastava, H.S., Patel, P.R., Shukla, A., Shukla, A.K., 2014. Absolute radiometric calibration of FRS-1 and MRS mode of RISAT-1 synthetic aperture radar (SAR) data using corner reflectors. Int. J. Adv. Eng. Res. Sci. 1 (6), 78–89.
Navneet, Sankarambadi, Kim, Jin-Woo, Zhong, Lu., 2017. A new InSAR persistent scatterer selection technique using top eigenvalue of coherence matrix. IEEE Trans. Geosci. Remote Sens. 56 (4), 1969–1978.
Papco, Juraj, Bakon, Matus, Kubica, Lukas, Belicova, Gabika, Droscak, Branislav, Ferianc, Martin, Rovnak, Martin, Ruiz, Antonio M., Sousa, Joaquim J., 2024. Satellite-based InSAR geodesy and collocation with GNSS. Procedia Comp. Sci. 239, 2329–2340.
Pawłuszek-Filipiak, Kamila, Wielgocka, Natalia, Tondaś, Damian, Borkowski, Andrzej, 2023. Monitoring nonlinear and fast deformation caused by underground mining exploitation using multi-temporal Sentinel-1 radar interferometry and corner reflectors: application, validation and processing obstacles. Int. J. Digit. Earth 16 (1), 251–271.
Pepe, Antonio, Solaro, Giuseppe, Calo, Fabiana, Dema, Claudio, 2016. A minimum acceleration approach for the retrieval of multiplatform InSAR deformation time series. IEEE J. Select. Top. Appl. Earth Observ. Remote Sens. 9 (8), 3883–3898.
Piter, Andreas, Haghighi, Mahmud Haghshenas, Motagh, Mahdi, 2024. Challenges and opportunities of Sentinel-1 InSAR for transport infrastructure monitoring. PFG J. Photogram. Remote Sens. Geoinform. Sci. 92 (5), 609–627.
Qi, Zhiyong, Mao, Yanpian, Tang, Zhengyang, Li, Tao, Fang, Rongxin, Mou, You, Xuhuang, Du, Peng, Zongyi, 2025. Fusing BDS and dihedral corner reflectors for high-precision 3D deformation measurement: a case study in the Jinsha River reservoir area. Remote Sens. 17 (17), 3000.

Qiao, Haiwei, Zhang, Ping, Li, Zhen, Huang, Lei, Zhipeng, Wu, Gao, Shuo, Liu, Chang, Liang, Shuang, Zhou, Jianmin, Sun, Wei, 2024. Snow depth retrieval method for PolSAR data using multi-parameters snow backscattering model. ISPRS J. Photogramm. Remote Sens. 218, 136–149.
Qin, Yuxiao, Perissin, Daniele, Lei, Ling, 2013. The design and experiments on corner reflectors for urban ground deformation monitoring in Hong Kong. Int. J. Antennas Propag. 2013 (1), 191685.
Rohmer, Jeremy, Loschetter, Annick, Raucoules, Daniel, de Michele, Marcello, Raffard, Damien, Le Gallo, Yann, 2015. Revealing the surface deformation induced by deep CO2 injection in vegetated/agricultural areas: the combination of corner-reflectors, reservoir simulations and spatio-temporal statistics. Eng. Geol. 197, 188–197.
Sarabandi, Kamal, Chiu, Tsen-Chieh, 1996. Optimum corner reflectors for calibration of imaging radars. IEEE Trans. Antennas Propag. 44 (10), 1348–1361.
Schaufler, Stefan, Bauer-Marschallinger, Bernhard, Hochstöger, Simon, Wagner, Wolfgang, 2018. Modelling and correcting azimuthal anisotropy in Sentinel-1 backscatter data. Remote Sens. Lett. 9 (8), 799–808.
Schlögel, Romy, Thiebes, Benni, Mulas, Marco, Cuozzo, Giovanni, Notarnicola, Claudia, Schneiderbauer, Stefan, Crespi, Mattia, Mazzoni, Augusto, Mair, Volkmar, Corsini, Alessandro, 2017. Multi-temporal X-band radar interferometry using corner reflectors: application and validation at the Corvara landslide (Dolomites, Italy). Remote Sens. 9 (7), 739.
Schwerdt, Marco, Schmidt, Kersten, Ramon, Núria Tous, Klenk, Patrick, Yague-Martinez, Nestor, Prats-Iraola, Pau, Zink, Manfred, Geudtner, Dirk, 2017. Independent system calibration of sentinel-1B. Remote Sens. 9 (6), 511.
Shi, Xuguo, Zhang, Lu, Balz, Timo, Liao, Mingsheng, 2015. Landslide deformation monitoring using point-like target offset tracking with multi-mode high-resolution TerraSAR-X data. ISPRS J. Photogramm. Remote Sens. 105, 128–140.
Silva, Alberto S., Sousa, Mário E.S., Braga, Eduardo M., Reis, Marcos A.L., 2024. Morphological and doping effects on electrical conductivity of aluminum metal substrate through pulsed electrodeposition coating of Cu-MWCNT. Metals 14 (9), 1060.
Singleton, A., Li, Z., Hoey, T., Muller, J.-P., 2014. Evaluating sub-pixel offset techniques as an alternative to D-InSAR for monitoring episodic landslide movements in vegetated terrain. Remote Sens. Environ. 147, 133–144.
Spencer, Roy C., 1944. Optical Theory of the Corner Reflector. Radiation Laboratory, Massachusetts Institute of Technology.
Talib, Oliver-Cabrera, Shimon, Wdowinski, Sarah, Kruse, Tonian, Robinson, 2022. Detection of sinkhole activity in West-Central Florida using InSAR time series observations. Remote Sens. Environ. 269, 112793.
Tan, Hong, Hong, Jun, 2016. Calibration of compact polarimetric SAR images using distributed targets and one corner reflector. IEEE Trans. Geosci. Remote Sens. 54 (8), 4433–4444.
Uhlemann, Sebastian, Chambers, Jonathan, Wilkinson, Paul, Maurer, Hansruedi, Merritt, Andrew, Meldrum, Philip, Kuras, Oliver, Gunn, David, Smith, Alister, Dijkstra, Tom, 2017. Four-dimensional imaging of moisture dynamics during landslide reactivation. J. Geophys. Res.: Earth Surf. 122 (1), 398–418.
Ulander, I.M.H., 1991. Accuracy of using point targets for SAR calibration. IEEE Trans. Aerosp. Electron. Syst. 27 (1), 139–148.
Ullah, Muhammad Ubaid, Latef, Tarik Bin Abdul, Othman, Mohamadariff, Hussein, Mousa I., Alkhoori, Hamad M., Yamada, Yoshihide, Kamardin, Kamilia, Khalid, Raheela, 2024. A progression in the techniques of reducing RCS for the targets. Alex. Eng. J. 100, 153–169.
Van Zyl, J., Jakob., 1990. Calibration of polarimetric radar images using only image parameters and trihedral corner reflector responses. IEEE Trans. Geosci. Remote Sens. 28 (3), 337–348.
Volakis, John Leonidas, Volakis, John Leonidas, 2007. Antenna engineering handbook, vol. 1755. McGraw-Hill, New York.
Wacquier, Loris, Whiteley, J., Gunn, D., Dashwood, B., Chambers, J., Watlet, A., Trafford, A., Donohue, S., 2021. Time-lapse monitoring of moisture induced landslide using surface waves at Hollin Hill landslide obsevatory. In: NSG2021 27th European Meeting of Environmental and Engineering Geophysics.
Wang, Suyun, Chen, Kun-Shan, Sato, Motoyuki, 2020. Performance of SAR polarimetric calibration using hybrid corner reflectors: numerical simulations and experimental measurements. IEEE J. Select. Top. Appl. Earth Observ. Remote Sens. 14, 440–451.
Wang, Xinyue, Yang, Zhoudong, Wang, Boya, Chen, Wei, Zhang, Guoqi, Zhang, Jing, Fan, Jiajie, Liu, Pan, 2023. Effect of epoxy resin addition on properties and corrosion behavior of sintered joints in power modules serviced offshore. J. Mater. Res. Technol. 25, 6593–6612.
Wang, Xu, Wang, Mingnian, Jiang, Ruolan, Jiani, Xu, Li, Bingtian, Wang, Xiao, Jianle, Yu, Pengfei, Su, Liu, Chaopeng, Yang, Qianru, 2024. Structural deformation monitoring during tunnel construction: a review. J. Civ. Struct. Heal. Monit. 14 (3), 591–613.
Xia, Zhuge, Motagh, Mahdi, Li, Tao, 2022. Performance analysis of dihedral corner reflectors for slope movements: a case study from Aniangzhai landslide in China. IEEE Geosci. Remote Sens. Lett. 19, 1–5.
Xing, Xue-min, Zhu, Jian-jun, Wang, Yong-zhe, Yang, Ya-fu, 2013. Time series ground subsidence inversion in mining area based on CRInSAR and PSInSAR integration. J. Cent. South Univ. 20 (9), 2498–2509.
Xing, Xue Min, Yuan, Zhi Hui, Chen, Li Fu, 2016. Highway deformation monitoring based on CRInSAR technique. In: 2016 IEEE International Geoscience and Remote Sensing Symposium (IGARSS).
Xing, Xuemin, Wen, Debao, Chang, Hsing-Chung, Chen, Li Fu, Yuan, Zhi Hui, 2018. Highway deformation monitoring based on an integrated CRInSAR algorithm — simulation and real data validation. Int. J. Pattern Recognit. Artif. Intell. 32 (11), 1850036.
Yang, Mengshi, Dheenathayalan, Prabu, López-Dekker, Paco, van Leijen, Freek, Liao, Mingsheng, Hanssen, Ramon F., 2020. On the influence of sub-pixel position correction for PS localization accuracy and time series quality. ISPRS J. Photogramm. Remote Sens. 165, 98–107.
Yu, Bing, Liu, Guoxiang, Li, Zhilin, Zhang, Rui, Jia, Hongguo, Wang, Xiaowen, Cai, Guolin, 2013. Subsidence detection by TerraSAR-X interferometry on a network of natural persistent scatterers and artificial corner reflectors. Comput. Geosci. 58, 126–136.
Zhang, Y., Wei, J., Duan, M., Kang, Y., He, Q., Wu, H., Lu, Z., 2022. Coherent pixel selection using a dual-channel 1-D CNN for time series InSAR analysis. Int. J. Appl. Earth Obs. Geoinf. 112, 102927.
Zhang, Wanye, Li, Xiaolu, Lu, Fei, Wei, Guoying, Liu, Jiao, Chen, Junfu, Ji, Cuiping, 2025. Electrophoretic deposited dual-functional composite coating for enhanced electrical insulation and anti-corrosion on 5052 aluminum alloy. Surf. Coat. 513, 132509.
Zhao, Feng, Mallorqui, Jordi J., 2019. A temporal phase coherence estimation algorithm and its application on DInSAR pixel selection. IEEE Trans. Geosci. Remote Sens. 57 (11), 8350–8361.
Zhao, Siyuan, McClusky, Simon, Cummins, Phil R., Miller, Meghan S., 2024. Co-seismic and post-seismic deformation associated with the 2018 Lombok, Indonesia, earthquake sequence, inferred from InSAR and seismic data analysis. Remote Sens. Environ. 304, 114063.
Zheng, Xiangtian, Yang, Xiaolin, Ma, Haitao, Ren, Guiwen, Zhang, Keli, Yang, Feng, Li, Ce, 2018. Integrated ground-based SAR interferometry, terrestrial laser scanner, and corner reflector deformation experiments. Sensors 18 (12), 4401.
Zhou, Yiao, Wang, Huiqi, Wang, Junying, 2024. Composite graphene-modified aluminum foil cathode current collectors for Lithium-ion battery with enhanced mechanical and electrochemical performances. Batteries Supercaps 7 (6), e202400028.
Zhou, Chao, Ye, Mingyuan, Xia, Zhuge, Wang, Wandi, Luo, Chunbo, Muller, Jan-Peter, 2025. An interpretable attention-based deep learning method for landslide prediction based on multi-temporal InSAR time series: a case study of Xinpu landslide in the TGRA. Remote Sens. Environ. 318, 114580.
Zhu, Jianjun, Wang, Changcheng, Yi, Heng, 2011. A new method for CR point identification and it's application to highway deformation monitoring. Geomat. Inf. Sci. Wuhan Univ. 36 (6), 699–703.